



AFRL-AFOSR-UK-TR-2013-0055



Particle-based Nano-Antennas at the Vis-NIR regime

Meier Orenstein

**Technion R&D Foundation
Senate Building Rm 157
Haifa 32000
ISRAEL**

EOARD Grant 10-3097

Report Date: November 2013

Final Report from 1 September 2010 to 31 August 2013

Distribution Statement A: Approved for public release distribution is unlimited.

**Air Force Research Laboratory
Air Force Office of Scientific Research
European Office of Aerospace Research and Development
Unit 4515 Box 14, APO AE 09421**

REPORT DOCUMENTATION PAGE				Form Approved OMB No. 0704-0188	
<p>Public reporting burden for this collection of information is estimated to average 1 hour per response, including the time for reviewing instructions, searching existing data sources, gathering and maintaining the data needed, and completing and reviewing the collection of information. Send comments regarding this burden estimate or any other aspect of this collection of information, including suggestions for reducing the burden, to Department of Defense, Washington Headquarters Services, Directorate for Information Operations and Reports (0704-0188), 1215 Jefferson Davis Highway, Suite 1204, Arlington, VA 22202-4302. Respondents should be aware that notwithstanding any other provision of law, no person shall be subject to any penalty for failing to comply with a collection of information if it does not display a currently valid OMB control number.</p> <p>PLEASE DO NOT RETURN YOUR FORM TO THE ABOVE ADDRESS.</p>					
1. REPORT DATE (DD-MM-YYYY) 29 November 2013		2. REPORT TYPE Final Report		3. DATES COVERED (From – To) 1 September 2010 - 31 August 2013	
4. TITLE AND SUBTITLE Particle-based Nano-Antennas at the Vis-NIR regime			5a. CONTRACT NUMBER FA8655-10-1-3097		
			5b. GRANT NUMBER Grant 10-3097		
			5c. PROGRAM ELEMENT NUMBER 61102F		
			5d. PROJECT NUMBER		
6. AUTHOR(S) Meier Orenstein			5d. TASK NUMBER		
			5e. WORK UNIT NUMBER		
7. PERFORMING ORGANIZATION NAME(S) AND ADDRESS(ES) Technion R&D Foundation Senate Building Rm 157 Haifa 32000 ISRAEL			8. PERFORMING ORGANIZATION REPORT NUMBER N/A		
9. SPONSORING/MONITORING AGENCY NAME(S) AND ADDRESS(ES) EOARD Unit 4515 APO AE 09421-4515			10. SPONSOR/MONITOR'S ACRONYM(S) AFRL/AFOSR/IOE (EOARD)		
			11. SPONSOR/MONITOR'S REPORT NUMBER(S) AFRL-AFOSR-UK-TR-2013-0055		
12. DISTRIBUTION/AVAILABILITY STATEMENT Distribution A: Approved for public release; distribution is unlimited.					
13. SUPPLEMENTARY NOTES					
14. ABSTRACT This is the final report for a grant covering research across a broad domain of metamaterial-based antenna research at the visible and near-infrared range (600nm to 2000nm), culminating in 38 peer-reviewed papers. The research covers elements of metamaterial-based antennas and antenna arrays in semiconductor devices, attempting to understand geometric effects of the unit cell on metamaterial performance and then translating this knowledge into design principles. The metamaterial-based antenna research is divided into five broad sub-areas: resonance tuning for concave antennas, capacitive versus conductive coupling, on-demand design (termed 'popcorn' antennas), broadband plasmonic metamaterials, and light focusing/energy harvesting by plasmonic antennas. The research on antenna arrays is divided into enhancement of organic solar cells by antenna arrays, applications of antenna arrays to speed LED response, current injection using antenna metamaterials, and the implementation of an enhanced short-wave infrared (SWIR) quantum cascade detector.					
15. SUBJECT TERMS EOARD, Metamaterials, nanoantennas, near-infrared					
16. SECURITY CLASSIFICATION OF:			17. LIMITATION OF ABSTRACT SAR	18. NUMBER OF PAGES 62	19a. NAME OF RESPONSIBLE PERSON Victor Putz
a. REPORT UNCLAS	b. ABSTRACT UNCLAS	c. THIS PAGE UNCLAS			19b. TELEPHONE NUMBER (Include area code) +44 (0)1895 616013

Final technical report

Particle-based Nano- Antennas at the Vis–NIR regime

Grant EOARD # FA8655-10-1-3097

Prepared for

AIR FORCE OFFICE OF SCIENTIFIC RESEARCH

AIR FORCE RESEARCH LABORATORY – DAYTON, OH

MAFAT INFRASTRUCTURE

For the period

September 2010 August 2013

Submitted by

Meir Orenstein, Principle Investigator



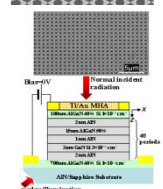
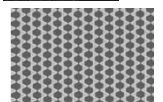
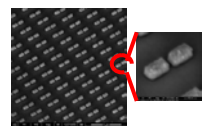
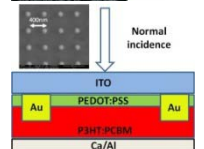
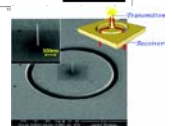
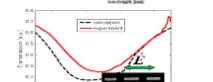
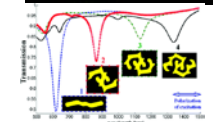
Nano/Micro Photonics Laboratory
Electrical Engineering Department
Technion – Israel Institute of Technology



Particle-based Nano- Antennas at the Vis–NIR regime

Final report (2010-2013)

Contents:	page
1. Abstract.....	3
2. Introduction.....	4
3. Antenna based metamaterial at the NIR-SWIR.....	6
i. Tuning the resonances (concave antennas).....	6
ii. 'Capacitive' vs. 'conductive' coupling (H antennas)..	11
iii. On-demand design ('pop-corn' antennas).....	16
iv. Broadband plasmonic metamaterials.....	21
v. Light focusing by a plasmonic antennas.....	28
4. Antenna arrays in semiconductor devices.....	32
i. Organic solar Cell enhanced by antenna array.....	32
ii. Faster LED by antenna array.....	39
iii. Antenna metamaterial for current injection.....	44
iv. Enhanced SWIR GaN quantum cascade detector.....	48
5. Summary and Outlook.....	54
6. Publications list from the project.....	55



1. Abstract

The research on the "Particle-based Nano-Antennas at the Vis–NIR regime" started at the time where metamaterials reached its peak popularity and was accompanied by a bazar of bizzar unit cell shapes and applications. With envisioned application field of enhanced miniatre semiconductor devices, this project had two goals: First: establish the understanding of the effect of geometry of the unit cell on the metamaterial perfrmance (spectral, enhancement) and translate it to design principles. We were focused in the wavelength regime of 600nm to 2000nm where most of the detection/emission of these devices occur. We believe that we accomplished this goal and we throughly understand the mechanism and comprehend the design concepts in detail. The second facet was the investigation of basic issues of productive combining of the above designed metamaterials into active semiconductor devices. In most previous cases metamaterials were implemented on passive substarte (e.g. glass) or if on a device – the device was usually optically operated (pumped). We were able to design, make and measure several types of real working devices (PV solar, LED and Quantum Cascade Detector) with an enhancing metamaterial layer. We believe that we are much closer now to possible actual realization of real-world efficient metamaterial enhanced semiconductor devices – and we are persuing further the understanding of the last barriers of this direction.

I want to acknowledge the generous support of AFOSR, AFRL and Mafat Infrastructes, which enabled achieving these results and I would like to thank the people who were involved in the initiation of the project and made it possible (Dr. Harold Weinstock, Dr. Ruth Pachter Dr. Lea Singer and Dr. Shlomo Zach) and to the assistance of the European office - the EOARD.

2. Introduction

a. Structure

The project is funded by AFOSR, AFRL and Israeli Ministry of Defense - MAFAT. The project collaborator and adviser is Prof. Nader Engheta (University of Pennsylvania).

In the course of the first year of the project, 6 graduate students were involved (Pavel Ginzburg, Nikolai Berkovitz, Iddo Dukman, Amir Nevet, David Arbel, Ophir Sorias) and a process engineer (Andrea Peer). Additional partial collaborations on some of the subjects were taking place with Prof. Nir Tesler - EE Dept. Technion on Organic PV, Prof. Gad Bahir – EE Dept. Technion on the GaN Quantum Cascade Detectors and Prof. Uriel Levi - Appl. Physics, HUJI on focusing configuration.

b. Summary of research

Metamaterials in the optical – NIR – SWIR regimes are predominantly based on realizations of metallic nano-circuits in each unit cell of the material. The emphasis of this research is not on the exotic regime of negative index of refraction, cloaking etc. but rather on resonant field enhancement and light storage and their possible applications. We believe that applications of this direction are imminent.

In the metamaterials field – many researchers dwell on the resonance characteristics of the nanocircuit within each unit cell, and much less on the fact that such a unit cell has to be also an efficient antenna – since the field is not directly fed into the optical circuit (as done in electronic circuitry), but rather is received by this antenna. Understanding the notion of a metamaterial as based on multiple resonant antennas, assists in design the material response.

We first studied theoretically and experimentally basic characteristics of the nanoparticles based antennas and their design rules, and subsequently looked on the (nontrivial) combination of the nanoantennas with semiconductor based devices, showing that such a combination – requires expanding our understanding on nanoantennas and novel design concepts.

We showed that the nano-antenna resonance can be tuned over hundreds of nanometer just by changing the local nature of the particle surface, and without modifying its cross section / aspect ratio, a feature which is highly important for realizing metamaterials. We further looked at the major differences between capacitive versus conductive coupling of antenna pairs. Finally we showed a method, allowing us to predesign any resonance for a nanoparticle (in fact any 2 characteristic parameters of the antenna, e.g. dipole and quadrupole resonances, can be determined independently), resulting in what we denote as a popcorn particle. We investigated the possibility of

nanoantennas for broadband (hundreds of nanometers) detection – and we showed that the concept of antenna hybridization (molecular like coupling) is not adequate for some coupled antenna scenarios – and we used this failure to generate broad band nanoantennas. Finally we looked at the focusing properties of such antennas.

Embedding our metamaterials – comprised of well-tuned nano-antenna arrays - in semiconductor based devices was investigated examining the combined merit of efficient antenna reception and light stoppage (light capacitor) as realized in well-designed nano antennas. We showed that such metamaterial can assist in photovoltaic enhancement via antenna based effects (directed-transmission and patch antenna) and by the stopped light effect (capacitor). We made the first organic based solar cell where the active organic semiconductor was modified to be an engineered metamaterial, resulting in enhanced performance. In a different experiment we realized the first metamaterial-communications-wavelength LED, where the emitting layer was coupled to a metamaterial layer. The measured emission rate exceeded substantially that of the non-radiative processes, enabling potentially high speed modulation (few GBits/sec) of this device – which may compete with a semiconductor laser. We looked at novel antenna designs for such electrically driven LED, where the location of the emitting layer and the antenna array should have distance separation in the order of 10 nm – thus modifying both the design concept of the semiconductor device layers as well as of the nanoantenna array. In a different experiment – we used another antenna based metamaterial to enhance the detectivity of a novel GaN based quantum cascade detector in the Swir regime, exploiting plasmonic based field rotation as well as plasmonic storage.

c. Outcome:

As a result of the project – 38 peer reviewed papers and conference proceedings were published and out of them including invited review paper and invited talks. Continuation projects were established – the main one is a large Israeli Government funded project: 'Nanophotonics for Detection and Sensing' directed by the PI of this AFOSR project – involving 14 research groups from Technion, TAU and HUJI.

2. Antenna based metamaterial at the NIR-SWIR regime

- i. Tuning the resonances: Concave Plasmonic Particles and Broad-Band Geometrical Tunability in the Near Infra-Red published in *Nanoletters* 10 pp. 1405-1408 (2011)



Metallic nanoparticles have been widely studied due to their interesting optical properties associated with localized plasmon resonances. These resonances have a variety of practical and prospective applications including: enhanced sensing and spectroscopy, plasmonic biosensors, cancer imaging and therapy' building block of metamaterials, ability to redirect scattered light, plasmonic lasers, SPASERS enhanced nonlinearities, enhancement of radiation efficiencies, and much more. Typical metallic nanoparticle's geometries, such as spheres, disks, cups, and bow-ties on a quartz or glass substrate, exhibit resonances primarily in the 'visible' spectrum (below $1\mu\text{m}$). The extension of these resonances to the near infra-red (IR) regime ($1\text{--}2\mu\text{m}$) is of great importance for optical communications, bio-medical applications and much more. For these purposes several smart modifications of the particles' geometry should be applied, e.g.: coupled particles separated by only several nanometers, few-nanometers-thin nano-shells, and elongated particles with very large aspect ratios. However, the repeatable fabrication of such configurations is challenging and limiting their applicability. High aspect ratio (elongated) particles are also difficult to integrate as metamaterials' unit cells, since unit cell dimension should be substantially smaller than the light wavelength.

Here we present metamaterials based on concave plasmonic unit cells. The specific unit cells are comprised of nano-scale cylinders with cross sections varied between the more conventional convex to highly concave shapes. The resonances of such metamaterials are significantly modified by the convexity sign of the cylinder cross section. Large tunability (many hundreds of nanometers) is achieved by slightly tuning geometrical parameters of concave particles, which is feasible without either pushing the fabrication process to extremes (compared e.g. to few-nanometer-thin rings required for similar tunability range) or largely distorting the square unit cell proportions (such distortion enhances considerably the particle size which yields higher order excitations as well as in inter-cell coupling). We detail the experimental and numerical results and provide the conceptual interpretation of the resonances. Specifically, we show that concave particles with dimensional aspect ratios of ~ 1 can support selectable resonance wavelengths encompassing the whole near IR regime.

The metamaterial is comprised of gold nanoparticles' arrays, which were produced by lift technique, employing electron beam lithography (EBL) on a glass substrate covered with 30nm ITO layer to eliminate charging effects. The nanoparticles are separated by gaps of about 300nm in order to avoid coupling between adjacent unit cells. The thickness of the nanoparticles is 60nm and their lateral dimension is varied in the 100 nanometers regime. The measurement of these metamaterials is accomplished by illuminating them with polarized white light under normal incidence and by monitoring the spectral features of the transmitted light (Fig.1).

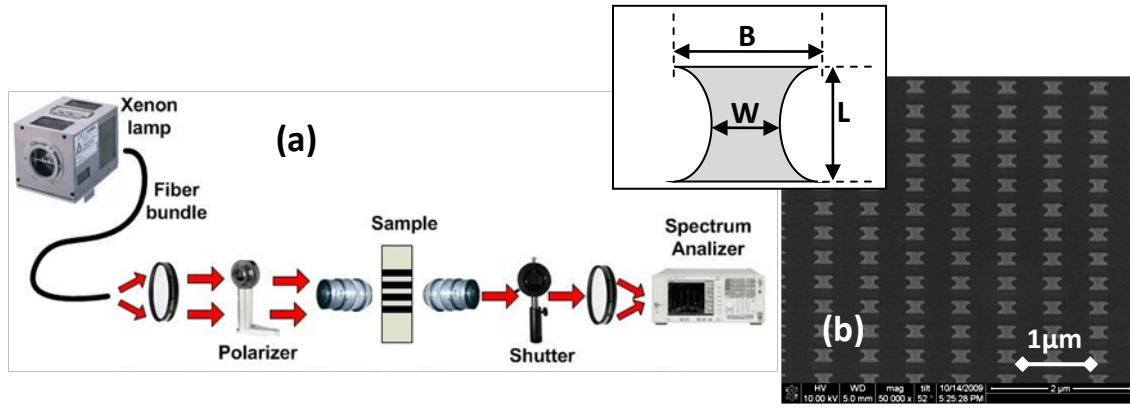


Figure 1. (a) Experimental setup (b) SEM image of concave nanoparticles based metamaterial; Inset shows the scheme of the concave hyperbolic particle

The localized plasmon resonance of a nanodisk is dependent on its geometry and dielectric properties of the disk and surrounding media. The resonance conditions of regular convex nanodisk can be analytically approximated as those of an ellipsoid with major axes a, b, c under Mie scattering:

$$\alpha_i = V \cdot \frac{\epsilon - \epsilon_m}{\epsilon_m + L_i (\epsilon - \epsilon_m)}, \quad i = a, b, c \quad (1)$$

where ϵ and ϵ_m are dielectric constants of the particle and the surrounding medium respectively, V the particle's volume, L_i the geometrical factor along the ellipsoid axis i , and α_i the polarizability tensor. In particular, we are interested in the normal incidence excitation of a fixed thickness ($h=60\text{nm}$) disk, starting with lateral diameter of 100nm (on a glass substrate with $n=1.5$). It is evident, that distorting the disk cross section by increasing the diameter parallel to the electrical field direction \vec{E} results in a red shift of the resonance, while enhancing the disk diameter in a perpendicular direction yields a small blue shift (Fig.2). In order to shift the basic plasmon resonance of a 100nm diameter Au sphere, located deep in the visible part of spectrum ($\sim 540\text{nm}$), to the center of the Near IR regime ($\lambda = 1550\text{nm}$), the sphere diameter should be distorted in the field direction to 420nm (aspect ratio of 4.2). Such a large ratio yields excitation of additional higher order modes (and retarded modes), as well as strongly couples between the metamaterial unit cells. Thus a simple distortion of a nanodisk cannot serve for affordable extreme tunability in near IR and another approach is requested.

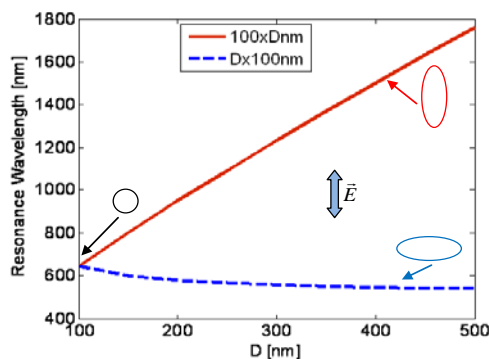


Figure 2. Influence of the geometrical factor on Mie resonance of the disk (numerical results of Eq.1). Red solid line – increasing the disk diameter D along the excitation polarization; blue dashed line – increasing the disk diameter D perpendicular to the excitation polarization. Arrow shows the polarization of the incident field

We propose here to employ the particle's concavity parameter to achieve large scale shifting and tuning of the plasmon resonance. In order to demonstrate the idea we fabricated metamaterials comprised of particles with a cross section of different convexities (and convexity signs). All particles have equal thickness (60nm) and similar lateral dimensions: central-width $W=100\text{nm}$, and length $L=250\text{nm}$; a concave (hyperbolic) particle has an additional parameter – base-width B (inset of Fig.1b for definition). The measured transmission spectrum with field polarized along the particle length is shown in Fig.3. A metamaterial with unit cell based on a particle with rectangular cross section (aspect ratio 2.5) exhibited a resonance at 1080nm. A convex cylinder unit cell (elliptical cross section with the same aspect ratio) had a slightly blue shifted resonance (1020nm), while even a slightly concave (hyperbolic) cylinder ($B=135\text{nm}$) exhibited a significant red shifted resonance (1180nm).

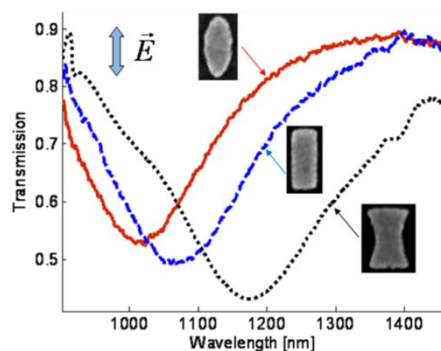


Figure 3. Measured transmission spectra of elliptical disk (red solid line), rectangle (blue dashed line), and concave hyperbolic particle (black dot line). Arrow shows the polarization of the incident field

For further investigation of the resonance tuning by the particle's concavity, we measured the resonance of concave hyperbolic particles as a function of the base-width B while keeping constant their central-width W and length L . The experimental results as well as numerical results by Finite Difference Time Domain (FDTD) are depicted in Fig.4. The dielectric constants of the materials, used in our FDTD simulation, are based on actual measured value for dispersion and losses. The resonance is considerably red-shifted (more than 350nm) by increasing the base-width of the concave particle (from 130 to 300nm). This result has an opposite trend compared to that obtained for convex disk particles, where enhancing the size of the particle perpendicular to the field polarization results in a small blue shift (Fig.2). Thus the red-shift encountered here is indeed related to the degree of concavity of the unit cell and not to increasing of the effective dimension (or area) of the particle.

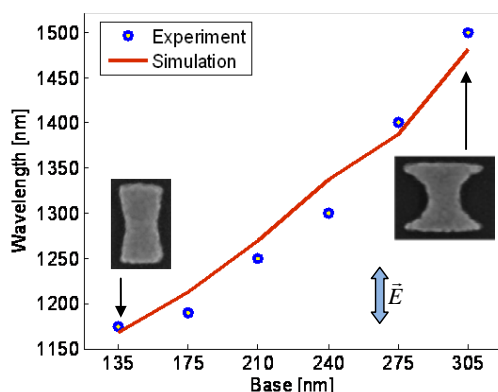


Figure 4. Resonance wavelength of metamaterials based on concave hyperbolic particles plotted as a function of its base-width B ; measured values (blue rings) and FDTD results (red solid line). Arrow designates the polarization of the incident field

The fundamentally different resonance behavior of convex and concave particles is related to the combination of global geometrical shaping of the surface charge distribution and the local geometry at points of high surface charge density. In the electro-quasi-static regime the geometry dependent eigen-solutions for the surface charge density and the eigen-values, related to the resonance frequency, are given by the following Fredholm integral equation:

$$\sigma(Q) = \frac{\varepsilon(\omega) - 1}{\varepsilon(\omega) + 1} \oint_S \sigma(M) \frac{\vec{r}_{MQ} \cdot \hat{n}_Q}{\pi |\vec{r}_{MQ}|^2} \cdot dS_M \quad (2)$$

where $\sigma(Q)$ is a surface charge density at point Q, $\varepsilon(\omega)$ the particle's dispersive dielectric constant, \vec{r}_{MQ} is a vector, connecting two points on the particle boundaries:

any point (M) with a point of interaction (Q), \hat{n}_Q is a normal to the boundary at the point Q, and the integration is performed on the particle boundary. Eq. 2 here is two-dimensional (for simplicity), while a full-fledged three-dimensional equation is written as a surface integral. It may be shown, that the resonance frequency for convex particles (as determined by the eigen-value $\lambda = [\varepsilon(\omega) - 1] / [\varepsilon(\omega) + 1]$) is bounded from below by geometrical factors, which necessitates very large aspect ratios in order to achieve near IR resonances. At these aspect ratios and for affordable fabrication parameters higher order resonances are invoked, and, furthermore, the quasi-static approximation may be invalid as well. However, this fundamental limit is not encountered for concave geometry, causing the substantial difference in resonance characteristics.

For the exact determination of the resonance frequency, Eq. 2 (or its 3D version) can be solved numerically. However the conceptual explanation for the concave particles resonance can be extracted from the structure of the integral of Eq. 2, and follows the rule that reduced interactions between the opposite sign surface charges – leads to red shift of the resonance. For concave particles, the normal to the surface can point in a counter direction to the charge separation vector, resulting in a local negative value of the scalar product within the integrand of Eq. 2, which yields a reduced value of the resonance frequency whenever a significant surface charge distribution is generated on the concave edges. This is exemplified schematically in Figs. 5(a)-5(c). The surface charge density is proportional to the discontinuity in the normal component of the electrical field. In Fig.5 (a) (convex particle), the two well defined groups of surface polarization charges are separated by vector \vec{r}_{MQ} , which is parallel to the surface normal (\hat{n}_Q), yielding a maximal value of interaction term $\vec{r}_{MQ} \cdot \hat{n}_Q$. This is directly related to a high resonant frequency, which can be red shifted to IR only by enhancing the separation between the charge distributions. For the rectangular case (Fig. 5(b)) the surface charges are distributed along the edge such that the contributions to integral (Eq. 2) incorporate also terms with reduced magnitudes due to both larger radius-vectors \vec{r}_{MQ} and misalignment with the surface charge distribution (the normal \hat{n}_Q). Thus, the resulting integral has a lower value yielding a

relative “red” shift. The most dramatic effect occurs for concave particles (Fig. 5(c)), where a significant part of the charge distribution is on the concave edges, resulting in a negative scalar product in the integrand of Eq. 2, namely “repulsion” type of interaction, leading to a substantial reduction of the resonance frequency even for aspect ratios of the order of unity.

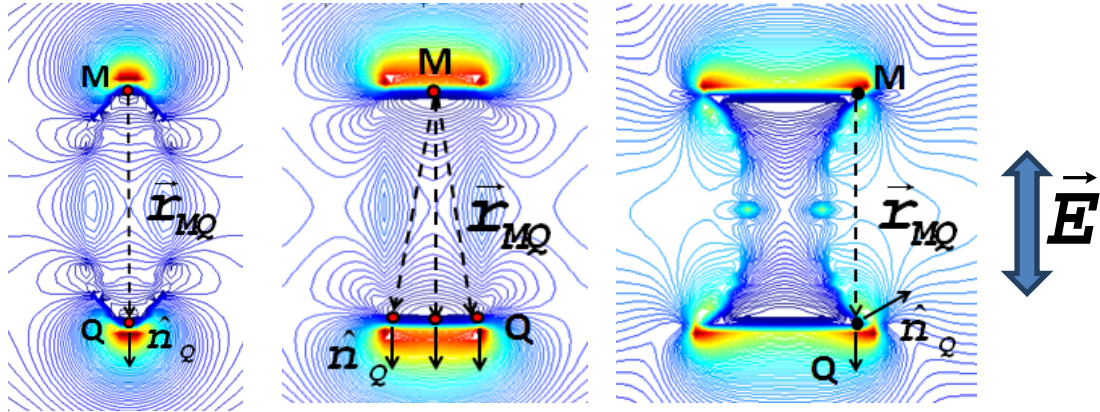
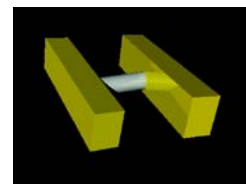


Figure 5. Calculated (FDTD) field distributions for particle with a cross section of (a) ellipsoid (b) rectangular (c) concave. Arrows and symbols are related to Eq.2

In conclusion, we showed experimental, numerical, and theoretical evidence, that concave nanoparticles with reasonably square-like aspect ratios exhibit broadly tunable resonances in the near IR. Design of particles, optimized for near IR resonances, relies on generation of substantial surface charge densities on the concave edges of the particle. These easily achievable IR resonances are favorable for a large span of applications.

ii. 'Capacitive' vs. 'conductive' coupling (H antennas): Thin wire shortening of plasmonic nanoparticle dimers
published in *Nanoletters* 11 pp. 2079-2082 (2011)



Ordered arrays of nanoparticles fabricated by means of Electron Beam Lithography (or similar methods) are of special interest, due to exact control of the size, shape, and relative position of the particles in array. It was also shown that arrays with closely spaced nanoparticles have different response to incident field than array with well isolated particles. Such difference was explained by mutual dipole interactions of the plasmon fields in adjacent nanoparticles. An extreme case occurs when the interparticle separation is reduced to zero thus generating a so called 'conductive' coupling. There are several conflicting measurements and interpretations of the characteristics of such touching particles. Some reports show an abrupt change of the scattering spectrum toward longer wavelengths attributed to the conductive contact. Yet other reports claim that the spectral transition accompanying the generation of a contact point is rather continuous and can be explained by simple dipolar interaction, although dipole approximation was shown to be typically invalid when interparticle separation is smaller than the particle diameter and multipolar terms should be considered. Another theoretical research shows that the spectral response of the touching particles depends on the junction geometry and can be red-shifted, continuous, and even blue-shifted. It should be emphasized that in many of the related references, the process of generating a conductive contact involves the moving of separated particles into close proximity, and furthermore to partial overlap. In this process, the capacitive interaction between the nanoparticles can become very strong and obscure the spectral shifts due to the formation of the conductive bridge between the particles. Furthermore, the scenario of partially overlapping particles entails also significant morphology change of the combined particle impeding the isolation of conductive coupling effect. Recently, few groups discussed theoretically a gradual transition from capacitive to conductive coupling by changing the conductivity of a connecting bridge between the particles with potential application for conduction sensor. Another work showed theoretically particles and particles' chains in strong coupling regime (separation gap of 20nm) connected by conductive bridge.

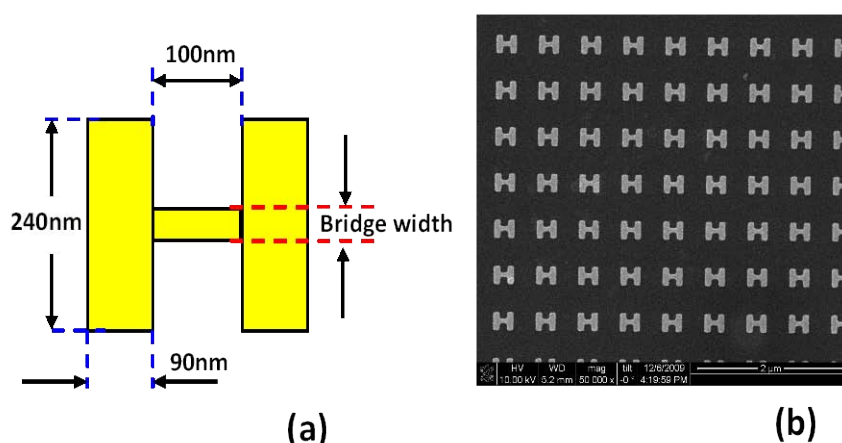


Figure 1. (a) Scheme of the particles connected by conductive wire (b) SEM image of a connected nanoparticles' array

We present experimental and theoretical study of metallic nanoparticles in the conductive regime. In order to distinguish between the effects related to the capacitive coupling and conductive coupling between the particles, the experiments were performed on pairs of metal nanoparticles separated by a large gap, and a narrow shortening wire was applied between them. We show that characteristics of the dimers with such conductive coupling differ significantly from those of the regular capacitive coupling which is manifested by an abrupt spectral shift of the plasmon resonance (more than 900nm), complete redistribution of the surface charges, and an improved intensity enhancement by an order of magnitude. Moreover, we show that the resonance wavelength and intensity enhancement can be tuned by slightly changing the width of the shortening bridge. As a general conclusion, the resonance characteristics after establishing even the tiniest conductive bridge are primarily determined by the ability of the surface charge to redistribute over the surfaces of the whole combined structure.

Before proceeding, it is essential to clarify the 'conductivity' notion. Although conductive coupling, charge transfer dimers etc. are commonly used in this field, due to similarity of these nanoplasmonic structures to regular circuit elements connected by conductive wire or to charge transfer molecular complexes, it is important to say that we are not dealing with real conductivity. The metal particles are predominantly dipolar materials at the optical frequencies (their losses (real conductivity) are definitely not the main effect determining the resonances). The 'conductive' wire is thus not the equivalent of a DC conductor and the 'current' flowing in the structure is rather a displacement (dipole) current, while the notion of high conductivity here is related to high value of the material dipole moment (real part of the electric susceptibility).

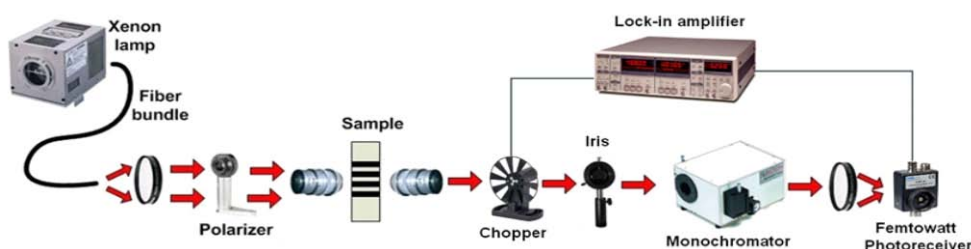


Figure 2. Experimental setup

To eliminate the influence of strong capacitive coupling on the conductive regime, we investigated the plasmon resonances of two rectangular Au nanoparticles separated by a large 100nm gap. The lateral dimensions of the particles are 90x240nm, and their thickness is 60nm (Figure 1a). For such configuration the coupling between the particles is small (resonance shift of only about 30 nm from that of a single particle), thus by introducing the connecting wire we clearly see the influence of the conducting regime. Moreover, by changing the width of the conducting wire we also investigate the influence of the conducting wire parameters on the plasmon resonance of the whole structure. The experimental samples, consisting of 50x50 μm^2 arrays of Au nanoparticle dimers (shortened and non shortened) (Figure 1), was produced by lift-off technique using Electron Beam Lithography on a glass substrate covered with 30nm ITO layer to eliminate the charging effect. The spacing between the dimers was 300nm in order to avoid inter-elements coupling within the array. Note that although the thin ITO layer is

conductive, its conductivity (or plasma frequency) is not high enough to serve as a conductive bridge between the particles at optical frequencies. Optical scattering measurements were performed by impinging normally incident polarized white light and collecting the transmitted light spectrum by a lens with numerical aperture 0.85 using a phase-locking detection scheme (Figure 2). Polarization of the incident light was chosen to be parallel to the interparticle axis. For perpendicular polarization the behavior of particles in conductive regime was almost the same as in coupling regime as noted before.

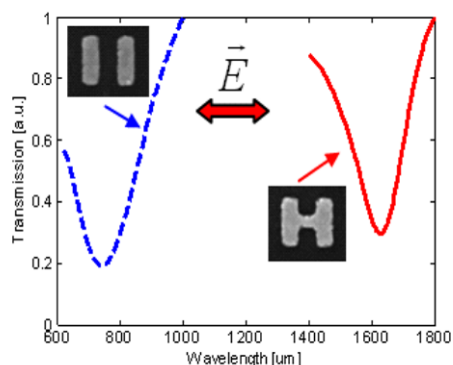


Figure 3. Transmission (forward scattering) spectra of the coupled and connected particles; bold arrow denotes the polarization of the excitation field

The Introduction of a narrow (60nm) conductive wire between the particles abruptly shifted the transmission (forward scattering) resonance of the dimer to the Near Infrared (NIR) part of the spectrum by more than 900 nm (Figure 3). It may be thought that by enhancing the ‘conductivity’ in the gap, namely increasing the wire width, we should expect a further red shift. But, as can be seen in Figure 4, the inverse effect occurs, and the spectral shift moderates as we enhance the wire width. Since the gap between the particles remains constant, the shift of the resonance wavelength is only due to the substantial redistribution of the surface charge to be much more delocalized now – thus contributing to the red shift. We also show a good correlation between the experimental data and simulations results of Finite Difference Time Domain (FDTD) – see simulation details below (Figure 4). In the simulation we calculated the shortening by even narrower wires (not shown in the figure) which gave the same trend e.g. a 10 nm wide wire shifted the resonance spectrum to 2500 nm. For narrower wires, in the few nanometer regimes – the use of the macroscopic Maxwell equations with bulk permittivity is not justified. Important to note is that geometry of our particles and of the connecting bridge is rectangular, namely, flat edges. For such a junction geometry a blue-shift of the resonance is predicted. The inverse (red) shift in our case emphasizes our general conclusion that the overall geometry of the combined particle is the main factor determining the spectral characteristics rather than only the junction structure.

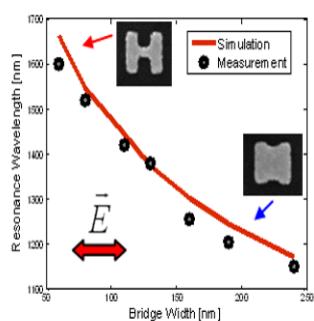


Figure 4. Resonance wavelength of the connected particles as a function of the bridge width; bold arrow denotes the polarization of the excitation field

In order to further comprehend the measured results we performed FDTD simulations for a single particle, coupled particles, and wire connected particles. The particles' parameters were chosen to be close to those of the experimental samples and the material data was taken from the literature. In Figure 5 we show the electrical field intensity of the particles at the forward scattering resonance. The field intensity on the particles edges is directly correlated to the surface charge distribution that defines the particle's resonance location. While the quasistatic approach is appropriately relating the red resonance shift to the concavity of the structure - for the size of our structures retardation effects have crucial contribution in determining the detailed field distribution and its enhancement. Of course the retardation effects are fully included in our calculations. For a single particle the dipole mode along the longer dimension is a more efficient scatter (Figure 5a) than the shorter dimension dipole (Figure 5b), and it is also manifested by larger intensity enhancement (about factor 10). For our weakly coupled dimer (100nm spacing) the field distribution for the perpendicular polarization is similar to that of the single particle with some small field modification on the inner edges due to weak dipole coupling between particles that also reduces the maximum intensity enhancement (Figure 5c). Parallel polarization yields field localization in the gap, but since the gap is large enough, the intensity enhancement is not much improved compared to a single particle (Figure 5d). But at the same polarization the characteristics of particles connected by a thin 60nm conductive wire are completely different. In this conductive regime the maximum of the field is located on the outer edges of the particles with almost no field in the gap (Figure 5f). Moreover, the intensity enhancement is about 20 times higher than that of the coupled particles (Figure 5d). This clearly suggests that connected particles cannot be viewed as coupled particles anymore. Therefore, one should rather examine the whole structure as a new composite particle, and deduce the resonance by the interaction of the local geometry with the surface charges. In particular, in the case of two relatively remote particles connected by thin wire, the combined particle is essentially partially concave, explaining the substantial red shift. Furthermore, when the shortening wire is wider, the delocalization of the surface charges is reduced (the distance between the main opposite surface charge distributions via the wider bridge is reduced) and the red shift is moderated. For perpendicular polarization there is almost no difference between the coupled (Figure 5c) and connected case (Figure 5e).

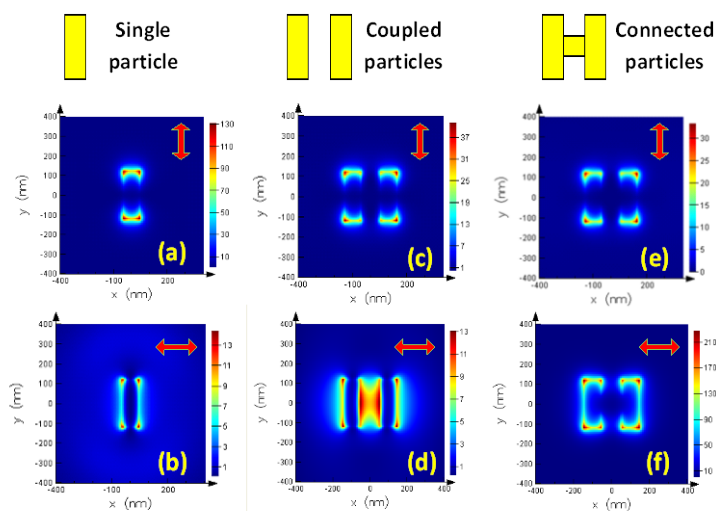
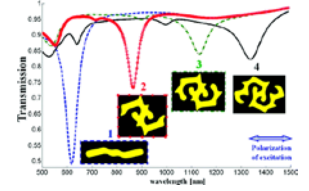


Figure 5. FDTD simulations results of the electrical field intensity for single particle (a), (b), coupled particles (c), (d), and connected particles (e), (f); bold arrow denotes the polarization of the excitation field. Note that the color intensity scales in not the same for the subfigures

As a general rule, the addition of a connecting wire between two particles is actually an addition of a bulk medium with strong dipoles. These dipoles compensate and eliminate the pre-existing surface charge (normal surface dipoles) at the connection points. If the wire is connected to the particles in a point where the pre-existing surface charge was substantial (e.g. our connected wire in the parallel polarization case), we expect to get a very large modification of the resonance characteristics.

In conclusion, we showed experimentally and theoretically the behavior of plasmonic nanoparticles shortened by a conductive wire. We showed that the behavior of particles in the conductive coupling regime is completely different than that in the capacitive coupling regime. We expect as a general rule that when two remote particles are shortened by a narrow wire, an abrupt red shift of the resonance will occur - resulting from the formation of an overall concave structure which is known to produce red shifted spectrum. The red shift will diminish as the shortening wire will become wider. This characteristic was well exemplified in our experiments and simulations. Such general behavior can be applied for the construction of metamaterials, engineering of plasmonic resonances, and in nonlinear optics. The very large shift of the resonance location obtained by very small ultra narrow metal connection can potentially be employed as a tool for remote spectral detection of shortened (here we mean real electrical shortening) microcircuits.

iii. On-demand design ('pop-corn' antennas)
published in *Nanoletters* 11 pp. 1329-1333 (2011)



Localized resonances of metal (plasmonic) nano-particles, stemming from the unique interplay between local geometry and dielectric dispersion, are already directed towards various novel applications. Although the task of designing nanoparticles with predetermined resonance wavelengths is of great interest, no generic method was hitherto presented. The existing methods for resonance engineering rely on parametric variation of certain dimension of a specific particle, or inter-particle coupling distance, but may be constrained by technological limitations. While evolutionary algorithms of different types are widely used in electromagnetic research for optimization on excitation signal for a given shape and for antenna engineering, they were not implemented in the field of nanoplasmonics, to the best of our knowledge. Moreover, most of the existing algorithms are heuristic and, in principal, may not converge to an optimal solution.

Here we propose and demonstrate on-demand engineering of the multipole optical plasmon resonances of a sub-wavelength particle. The method is based on a series of small perturbations applied to an initial particle, which enables the modification of the spectral location of a resonance or multiple resonances according to specific predetermined values. Moreover, resonances of different multipole orders can be designed to be degenerated at specific wavelengths, e.g. the dipole and quadrupole resonances are collocated at the same wavelength. The various resonances and field distributions were calculated analytically by our method and subsequently verified using forward scattering finite difference time domain (FDTD) simulations.

Small perturbations of an initial particle geometry yield small shifts of its resonances. Here we show that a proper sequence of perturbations is capable of shifting the resonances towards the requested values. Since a resonance is determined by the material permittivity $\varepsilon(\omega)$ at the resonance frequency ω , the problem may be formulated in terms of $\varepsilon(\omega)$ rather than ω . Suppose that a pair of initial resonances $\varepsilon_1, \varepsilon_2$ of a polygonal shaped nano-particle should be shifted towards a new pair. The following perturbation will be applied – each side k of the initial polygon will be associated with a real number a_k . The side will then be moved in the direction of the local normal by a distance of $h \cdot a_k$, where h is a small dimensionless parameter, common to all sides. The formalism of resonance shifting due to such shape perturbation of a plasmonic particle yield:

$$\frac{\partial \varepsilon}{\partial h} = (1 - \varepsilon) \frac{\int_{\partial \Omega} d^2 S a \left((\nabla_{\delta} u_{in})^2 + \varepsilon (\partial_n u_{in})^2 \right)}{\int_{\partial \Omega} d^2 S u_{in} \partial_n u_{in}} \quad (1)$$

where $\frac{\partial \varepsilon}{\partial h}$ is the derivative of the dielectric permittivity in respect to the dimensionless parameter h , u_{in} the electric potential inside the unperturbed particle, $\partial \Omega$ the particle boundary, ∂_n a derivative normal to the boundary direction, ∇_{δ} a

derivative tangent to the boundary direction, and a a scalar function along the boundary, indicating the amount of particle deformation in the direction of the local normal. Suppose that we move only two arbitrary sides on the discretized boundary by a fraction of $h \cdot a_1$ and $h \cdot a_2$ correspondingly, and consider the following measure

$S_{1,2} = \frac{\partial \varepsilon_{1,2} / \partial h}{(1 - \varepsilon_{1,2})} \int_{\partial \Omega} d^2 S u_{in} \partial_n u_{in}$. Only the sign of $S_{1,2}$ is of importance, since it indicates the direction of the eigenvalue modification after the applied variation. If any combination of signs is possible, it means that any pair of initial resonances may be shifted towards any independent location. Eq. 1 may then be rewritten as:

$$\begin{pmatrix} S_1 \\ S_2 \end{pmatrix} = \begin{pmatrix} \mu_1 + \varepsilon_1 \eta_1 & \mu_2 + \varepsilon_1 \eta_2 \\ \mu_1 + \varepsilon_2 \eta_1 & \mu_2 + \varepsilon_2 \eta_2 \end{pmatrix} \begin{pmatrix} a_1 \\ a_2 \end{pmatrix}, \quad \mu_{1,2} = (\nabla_{\partial} u_{in}(x_{1,2}))^2, \quad \eta_{1,2} = (\partial_n u_{in}(x_{1,2}))^2 \quad (2)$$

This equation is solvable for nondegenerate resonances, since the determinant of the matrix is not zero. Consequently, since the rank of the relevant geometrical transformation is 2, up to two nondegenerate eigenvalues (multipole resonances) may be moved towards any requested values. Specifically, any single resonance (dipole, quadrupole, etc) may be shifted as required.

For a given arbitrary shape (polygon) all the resonances may be calculated by solving the 'direct problem' of extracting the spectral eigen value for the resonances of a known geometry and material parameters. Here we used discretized boundary integral method, yielding a matrix equation for the eigen values (function of dielectric permittivity) and eigen vectors (surface charge distribution). Other solver including FDTD, finite element method, and volume integral method may be employed as well. In order to reduce the calculation complexity, we formulate the problem in two dimensions – infinite cylinder with polygonal cross section. Small perturbations to a particle geometry yield small shifts of its resonances, which are tracked by the 'direct solver'. Each applied perturbation requires verification of the shape validity according to topological and technological limitations: minimal angles (to avoid sharp corners), minimal width (to avoid high aspect ratios), and no-intersections. The perturbation is applied in the following way – two opposite sides of a symmetric shape are moved by a fraction δ in the direction of the local normal tilted by an angle θ (preserving the initial symmetry). θ is an additional degree of freedom used for faster convergence. The particle is subsequently smoothed to prevent corners. If the resulting shape satisfies the desired properties then all resonances are recalculated. The perturbation will be accepted if the resonances will move towards their required values, otherwise the perturbation is nullified and the algorithm step is repeated.

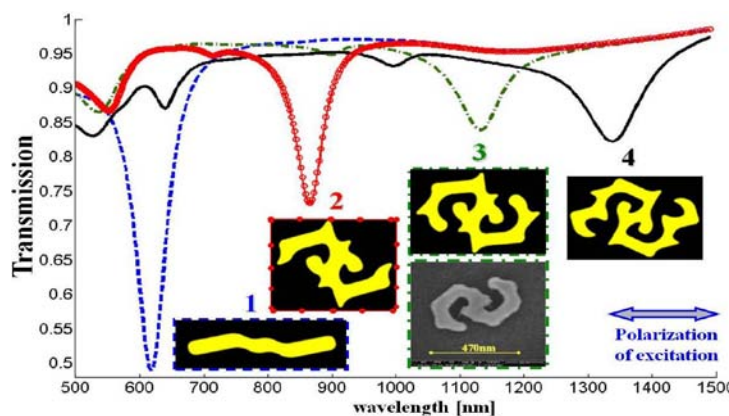


Figure 1. Transmission spectra of engineered particles. Insets – particles shapes: 1 – blue dashed line, 2 – red circles, 3 – green dash-dot, 4 – black solid. Arrow states for polarization of electrical field of the plane wave excitation. 3 (bottom) – SEM image of fabricated particle,

By applying this method we produced a series of particles with resonances spanning the entire visible and NIR spectrum and verified their transmission spectra by FDTD simulations using a proper excitation. These explicit examples show that the entire spectrum may be optimized for absorption and serve, for example, as a building block in solar cells and related applications. The transmission spectrum (forward scattering) of each particle is presented in Fig. 1, where the insets are the corresponding particle geometries and arrows correspond to the proper polarization of their excitation. This numerical experiment also corresponds to normal incidence spectroscopic measurements, using an array of particles rather than a single particle, in order to enhance the transmitted signal [16]. It should be noted that quality factors of plasmonic resonances, evaluated in our calculations to be ~ 20 , are usually limited to values below 100 and are higher at the visible spectrum than at NIR. However, the usefulness of the localized plasmon resonances does not emerge from their quality factor, but rather from their associated small modal volumes. The simulated particle transversal dimensions were taken to be 100nm in diameter (maximal distance between two points on the object); however, this parameter was found to have minor influence, since all the resonances have quasi-static characteristics. The particle material was chosen to be Au (including losses) with the measured dispersion function. Each transmission dip within the spectrum corresponds to an engineered dipole resonance and fits the values predicted by our method within $\sim 2\%$ accuracy. The resonances of convex gold particles with small aspect ratios are situated in the visible part of the spectrum; hence the shifting to longer wavelengths increases the number of required perturbations, as may be seen from the complexity of the final shapes (Fig. 1).

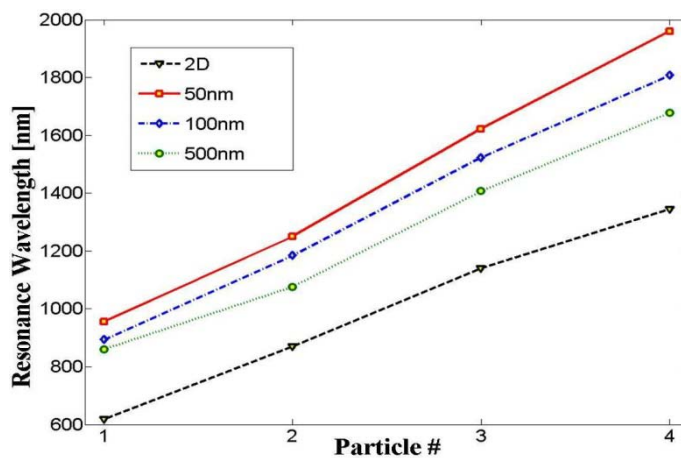


Figure 2. Resonances for 3D particles - infinite height (black triangle), 500nm (green circle), 100nm (blue diamond) and 50nm (red rectangle) thick disk particles. Particles numbers '1'-4' correspond to 'A'-D' particles from Fig. 1

Although we demonstrate the method for 2D particles in order to reduce the calculation time, it may be used in 3D, and is therefore a very powerful tool. Moreover, particles with cylindrical cross-section and finite height are of potential interest for applications and they may be related directly to 2D shapes with phenomenological Lorentz depolarization factor. According to this model - increasing a particle dimension in the direction of the excitation polarization shifts the particle resonance to the red, while if such an increase is made in the perpendicular direction, the particle's resonance exhibits a blue shift. We verified it by performing forward scattering simulations for particles of 50, 100 and 500nm height (Fig. 2). Very similar linear behavior of the resonance location was observed for all cases, exhibiting a red shift from the infinitely thick (2D) to the thin (50nm) particle, demonstrating that the

resonance location for this 3D scenario can be deduced to a good approximation from the 2D calculation.

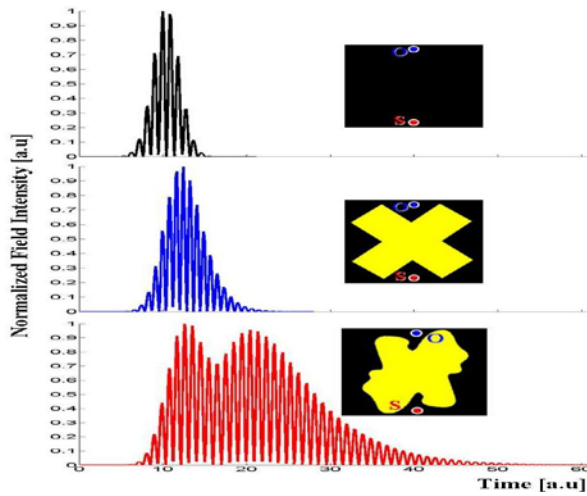


Figure 3. Normalized electrical field intensity of the function of time. (a) free space, (b) 'cross-shaped' particle, (c) 'degenerate-resonance' particle. 'S' is the dipole source location, 'O' is the observation point

To further exploit the capabilities of our method we generated a new family of particles in which two resonances of different orders are brought to be frequency degenerated at a desired wavelength. An initial 'cross-shaped' particle (inset of Fig. 3b) that exhibits dipole and quadrupole resonances separated by about 30nm (in 2D geometry), is mutated to a particle (inset of Fig. 3c) with the dipole (Fig.4 (a)) and quadrupole (Fig.4 (b)) resonances collocated at ~560nm. Particle parameters are similar to those of Fig. 1. This unique phenomenon may contribute to applications such as optimal nano-scale absorber, emitters' lifetime manipulation, and near field storage devices. To examine the unique behavior of such particles, we performed FDTD simulations, in which a dipole source was placed in the vicinity of each of the two particles: the perfect cross-shaped, and the above discussed 'degenerate-resonance' particle (marked by 'S' in insets of Fig. 3). The overall near-field intensity in the vicinity of each particle (marked by 'O' in insets of Fig. 3) was calculated as a function of time. Fig. 3a shows a time dependent field intensity of the excitation pulse, while Fig.3b shows the response of the 'cross-shaped' particle. Since only the 'bright' dipole mode of the structure was excited, the particle near field decays fast due to the efficient retransmission to the far field. On the other hand, the time response of the 'degenerate-resonance' particle (Fig.3c) is completely different, since its resonances are degenerated in frequency - dipole (bright) and quadrupole (dark) are simultaneously coupled to the excitation, creating a coherent superposition of two modes. Moreover, lifetime of the dark mode is much longer because of its reduced coupling efficiency to the far field.

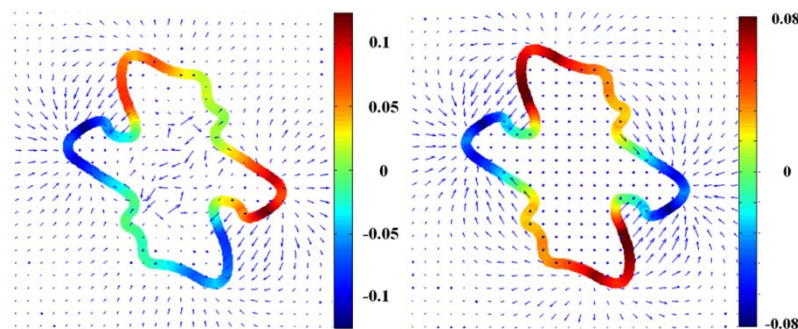


Figure 4. A particle with collocated resonances and the corresponding electrical fields. Color on the boundary indicates the surface charge distribution. (a) dipole, (b) quadrupole

Fabrication of these particles, resonant at NIR, is definitely feasible with today's mature nano-technology, although it may require advanced lithography such as E-beam lithography, including a correction of the proximity effect. All these significant issues were constrained in the algorithm, and eventually actually realized (inset of Fig.1) by lift-off technique, employing electron beam lithography (EBL) on a glass substrate covered with 30 nm Indium Tin Oxides (ITO) layer to eliminate charging effects. The thickness of the nanoparticles is 60nm. The width of the nanoparticle is about 70nm and the gaps inside particle are about 40nm wide. In order to eliminate proximity effects during the exposure of the particle, non-homogeneous dose of exposure was used.

In conclusion, we developed a generic method for the engineering of plasmon resonances which is capable of producing particles with desired resonances over the entire spectrum. Moreover, unique collocation of several resonances may be achieved and employed for storage of the near field energy and for absorption enhancement.

V. Broadband plasmonic metamaterials for the near infrared regime (to be submitted to Nanoletters)

Broadband plasmonic metamaterials for the near infrared regime are presented, based on a coupling of multiple small antennas in a unit cell. Design rules for building such metamaterials and overcoming the undesired coherent coupling followed by excitation of out-of-phase modes are presented. Dependence of metamaterial's response on separating gap between particles is shown experimentally and by finite difference time domain simulations.

Dipole plasmon resonances of the metallic nanoparticles are generally not narrow and resonance width exceeds 100nm. Width of the resonance has two major contributions – absorption losses and scattering losses. Absorption losses are more important for small (<50nm) nanoparticles while for larger nanoparticles the resonance shape is predominately determined by scattering phenomena. Wide width of the resonance is a disadvantage for applications such as sensing or plasmon rulers, therefore much narrower quadrupole or Fano resonance can be used for this purpose instead of regular dipole mode. On the other hand wide resonance might be an advantage for other applications such as filters or broadband metamaterials. In this work we present rules for building broadband metamaterials for NIR using near-field coupling between plasmonic nanoparticles. Influence of mutual orientation of particles and interparticle coupling within the metamaterial unit cell and between adjacent unit cells will be discussed.

Plasmon resonance of the single particle can be widely tuned within visible and NIR regimes. There are multiple ways to shift plasmon resonance of the nanoparticle: changing aspect ratio of the elongated particles, modifying particle's geometrical parameters such as concavity, coupling between several nanoparticles, hybridization of the nanoparticle modes in structures such as rings or shells, and modifying refractive index of the surrounding substrate and cladding materials. Using mentioned above recipes one can build efficient optical filters by utilizing periodic arrays of equal nanoparticles. Such arrays are simplest metamaterials that contain only one particle within the unit cell and can be tuned to any desired central wavelength by demand. But modification of the resonance shape in such single-particle metamaterials is problematic since the shape of the resonance is determined simultaneously with its location. In order to modify the spectral response of such metamaterials without moving the location of the central wavelength several scenarios can be used. The simplest scenario in terms of design is to combine several different single-particle arrays deposited in separated layers. For large separation distance between layers each array works independently from others and transmission function of the whole metamaterial will be easily deduced from transmission functions of its constituents. Disadvantage of this method is the fabrication process of the metamaterial since it includes several layers and thus very laborious. The more optimal scenario is to design single-layer metamaterial with unit cell that is capable to provide the desired functionality. In such metamaterial several nanoparticles should be included into the unit cell and in order to keep the total efficiency of the metamaterial the fill-factor of the particle's array should be increased, that will lead to unavoidable coupling between particles within the single unit cell and between the adjacent unit cells. Thus in order to derive design rules of building broadband

metamaterial for NIR we should understand the influence of interparticle and intercell electromagnetic coupling on the transmission spectrum.

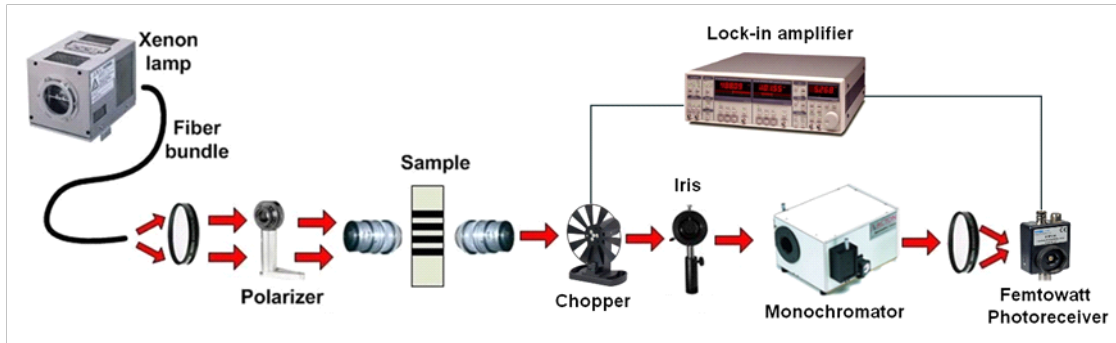


Figure 1. Experimental setup. Inset shows SEM image of the particles' array

In order to achieve spectral response in NIR regime we used elongated Au particles as building blocks of our metamaterial. Particle's arrays $50 \times 50 \mu\text{m}$ were fabricated by E-beam lithography method on a glass substrate with 30nm ITO layer used for eliminating charging effects and 5nm Ti layer for Au adhesion. Height of the particles is 50nm, their width 90nm, and their length was 280nm, 330nm, and 360nm for three types of particles respectively. Particles were characterized by measuring the normal incidence transmission spectrum in phase-locking detection scheme (Figure 1) and by simulation using commercial FDTD program (Lumerical).

We first start with the characterization of the stand-alone particles. In order to make coupling between adjacent particles negligible we made arrays of particles separated by 300nm gap in both directions. We used three different types of particles - with length of 280nm (L280), 330nm (L330), and 360nm (L360) respectively. Measured and simulation results are presented on Figure 2. Polarization of the excitation light was chosen to be along the longest dimension of the particles. Note that there is a good correlation between simulation and experiment spectra and such particles can be used as building blocks for broadband filters with central wavelength located within range 1200-1400nm.

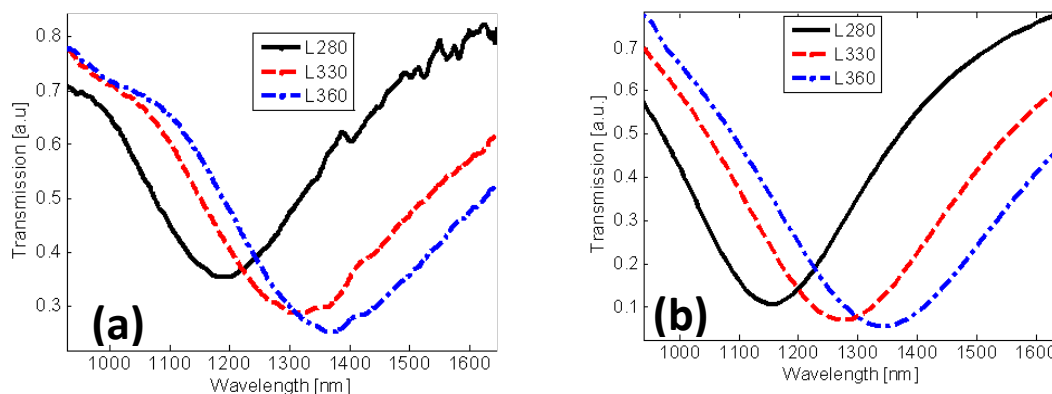


Figure 2. Experimental (a) and simulation (b) results of normal incidence spectra for particles with length of 280nm (black solid line), 330nm (red dashed line), and 360nm (blue dot line)

Now we investigate the coupling between different nanoparticles within single unit cell. Particle's dimer is a simplest example of interacting particles. We combine

within the unit cell particles with different length – L280 and L330 that were measured before. As it well known from hybridization theory the resulting hetero-dimmer has two dipole resonances that caused by in-phase and out-of-phase interaction of dipole moments of constituent particles. Mutual orientation of particles that constituent hetero-dimmer and the interparticle distance determine the interaction strength and the resulting resonance split. We will focus in two major configurations of the hetero-dimmer: parallel configuration, where elongated particles are coupled side-by-side (Figure 3a) and serial configuration, where such particles are coupled end-to-end (Figure 3b). In both configurations it is expected to see “bright” in-phase mode (σ and π^* states) and “dark” out-of-phase mode (σ^* and π states).

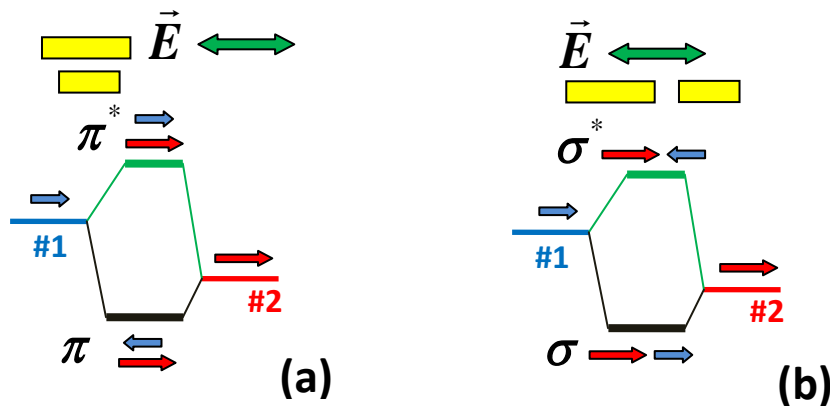


Figure 3. Energy scheme of the hybridization model for hetero-dimmer in (a) parallel configuration and (b) serial configuration

It should be noted, however, that for our purpose, namely broadband metamaterial, such resonance split caused by coupling is undesirable, since instead of combining two independent transmission functions into one broad band-pass filter we should always get two resonances: one broad superradiant resonance and another narrow subradiant resonance. Thus our investigation will be focused on possible solutions to reduce the coupling strength that causes the resonance split on the one hand, and not to decrease the value of the array fill-factor on the other hand. In order to avoid strong coupling between particles we will use moderate gap of 100nm between particles within the hetero-dimmer and large gap of 300nm between adjacent hetero-dimmers. The resulting spectrum of the hetero-dimmer in both configurations is presented on Figure 4. Parallel configuration of the hetero-dimmer is shown on Figure 4a. As expected, there are two minima in transmission spectrum - broad resonance at shorter wavelength that corresponds to superradiant in-phase mode π^* and narrow resonance at longer wavelength that corresponds to subradiant out-of-phase mode π . Subradiant resonance has smaller dipole moment thus its strength is much weaker than that of the superradiant mode. In the case of homo-dimmer, which consists of equal particles, the subradiant mode does not appear in transmission spectrum at all since equal out-of-phase dipole moments of constituent particles completely cancel it other. It should be also noted that although there is a good correlation between simulation and experimental data, the narrow subradiant resonance of the experimental spectrum is much less pronounced than in simulation because of additional broadening of the resonances caused by inhomogeneity of the fabricated particles array. The spectrum of the hetero-dimmer in serial configuration (Figure 4b) is quite different. Although it also has two minima as in the case of parallel configuration, their strength is about the

same and the whole spectrum seems much more symmetric. Additionally, despite the fact that the separating gap between particles in both configurations is the same (100nm) the resonance split of ~138nm in serial configuration is much smaller than that of the parallel case (~315nm) and is more similar to difference between resonances between stand-alone constituent particles L280 and L330 (~112nm). In order to explain the results we calculated the surface charge distribution on the hetero-dimmer particles at the resonance wavelengths. The results are presented on Figure 5. Surface charge of the hetero-dimmer in parallel configuration (Figure 5a) is completely matching the expectation. The broad resonance at the shorter wavelength is given by in-phase interaction between dipoles, whereas the weaker narrow resonance at the longer wavelength belongs to out-of-phase dipole arrangement. For the serial configuration, on the other hand, both resonances are determined by in-phase dipole arrangement that again resemble the charge distribution of the stand-alone particles – shorter wavelength resonance match the surface charge distribution of the shorter particle (L280) and longer wavelength resonance shows stronger dipole charge on a longer particle (L330). From the results presented on Figures 4 and 5 we can conclude that for serial configuration of the hetero-dimmer the expected resonance split with appearance of out-of-phase mode σ^* does not occur.

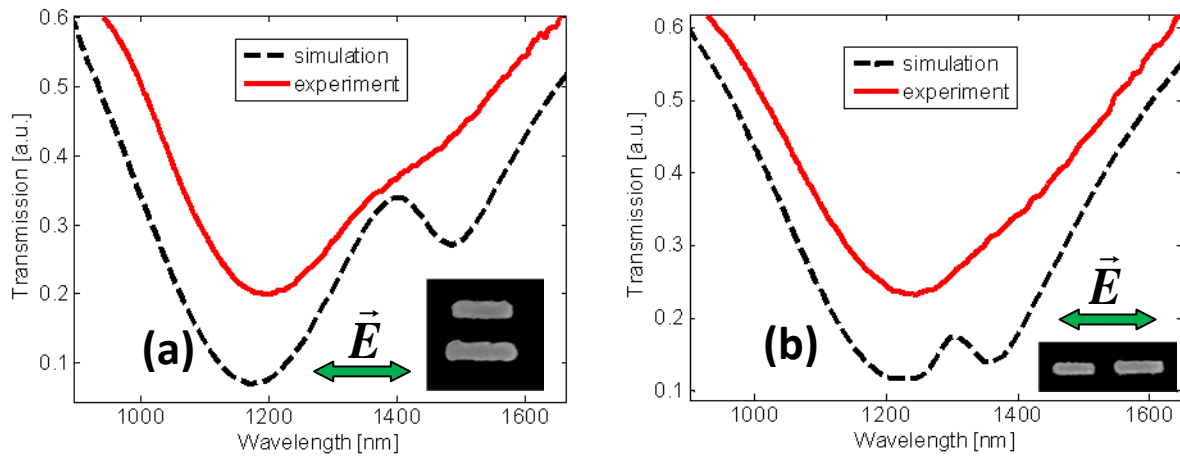


Figure 4. Simulation (black dashed line) and experimental (red solid line) spectra of the hetero-dimmer based metamaterial: (a) parallel configuration and (b) serial configuration. Insets show SEM images of the related hetero-dimmers.

The reason for disappearance of the mode σ^* in transmission spectrum is based on a symmetry breaking caused by the excitation field. Energy states of the hetero-dimmer that were shown on Figure 3 are only possible eigen-modes of the system, and the probability of excitation of the given mode is strongly dependent on the properties of the excitation. In both, FDTD simulation and normal incidence transmission experiment, the excitation is a linearly polarized electrical field that, compared to the size of nanoparticles, can be treated as a plane wave. For uncoupled particles such excitation generates dipole moments along the polarization direction of the excitation field in each of the particles of the hetero-dimmer. Since hetero-dimmer consists of two different types of particles, the resonance location of each particle will be different. At resonance of the first particle its dipole field will be much stronger than that of the second one. Consider such particle at the resonance with induced dipole moment along the particle's longest axis X by excitation field \vec{E}_{in} (Figure 6). For parallel configuration of the hetero-dimmer the second particle should be placed at the

point P (Figure 6). In such case the induced dipole field of the first particle at the point P will be in the opposite direction to the dipole moment of the second particle, thus creating possibility to reverse the direction of the second dipole (that is not in resonance) and building out-of-phase π state. For serial configuration the situation is different. Second particle should be placed at the point S (Figure 6), thus induced field of the first particle will be aligned along the dipole moment of the second particle and cannot reverse the direction of the second dipole. Therefore excitation of the out-of-phase mode σ^* is impossible for given linearly polarized plane wave excitation, and such serial configuration of the particles will be highly important for building broadband filters.

In order to emphasize the importance of the serial combination of the particles we made another metamaterials that based on unit cell that consists of three different particles. Additionally to previously used particles L280 and L330 we added another particle with length of 360nm (L360). As in hetero-dimmer metamaterial we keep gap of 100nm between particles within the unit cell and gap of 300nm between adjacent unit cells. The simulation and experimental spectrum of such metamaterial is shown on Figure 7. Parallel configuration of the unit cell (Figure 7a) shows the well defined resonance split caused by coupling between different nanoparticles. Such split results in strong and broad in-phase mode at shorter wavelength and in two much weaker out-of-phase modes located at the longer wavelengths. On the other hand, the serial configuration of the unit cell (Figure 7b) shows broad band-pass shape without undesired resonance splits and thus much more appropriate for building the broadband metamaterials.

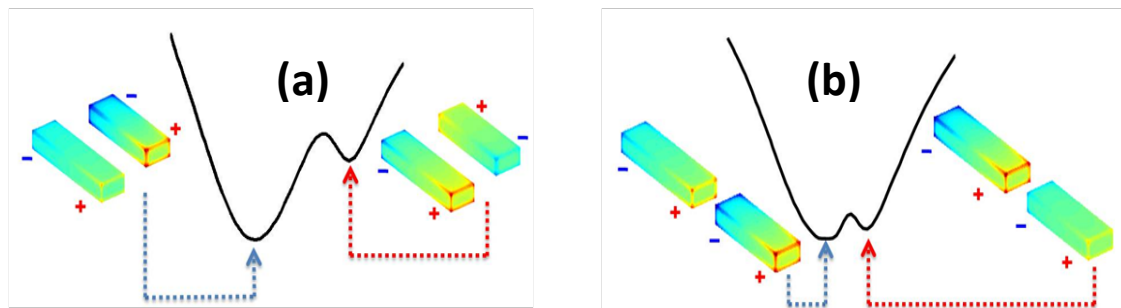


Figure 5. Normalized surface charge distribution on nanoparticles that constitute the hetero-dimmer in (a) parallel configuration and (b) serial configuration at resonance wavelengths

The last issue to be considered here is the influence of the distance between adjacent unit cells. Since serial configuration of the particles in unit cell was shown to be superior for broadband applications we will concentrate our study on coupling phenomena in metamaterials of the serial type (Figure 8). Horizontal gap Gap_H between adjacent unit cells can be of the same order as a gap between particles within the unit cell since in horizontal X direction the coupling between unit cells has also serial configuration and thus is less critical. On the other hand, the intercell coupling in Y direction, that is determined by Gap_V parameter, creates interaction in parallel configuration between unit cells (Figure 8), and thus potentially much more important for resonance shape and location. Interaction between different nanoparticles for

parallel configuration creates both in-phase and out-of-phase modes, but in the case of the interaction between identical unit cell out-of-phase configuration will be “dark” mode and thus will not be excited by far field excitation. Therefore, influence of the intercell coupling in vertical Y direction will results in resonance blue-shift toward “bright” in-phase mode only. The strength of the coupling, expressed in terms of the resonance shift, is dependent on gap between unit cells and on geometry of the particles. For point dipoles such interaction is generally approximated by near-field $1/d^3$ term, where d is a distance between dipoles.

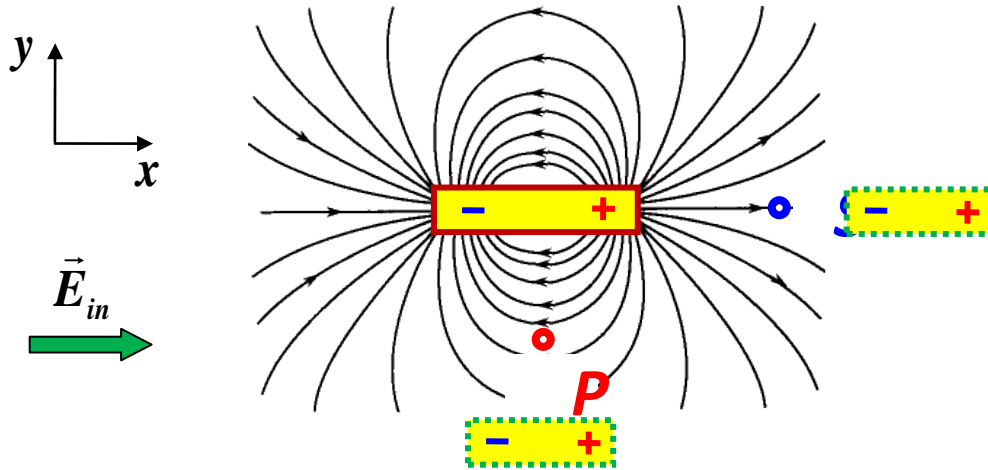


Figure 6. Near field lines of the dipole moment that is excited in the rectangular nanoparticle by x-polarized incident excitation field. Points S and P show the position of the additional particle in the hetero-dimmer for serial and parallel configurations.

For nanoparticles with size of about 100nm and bigger, the dependence is different. In order to check the strength of such interaction we made two samples: the first consists of square 100x100nm nanoparticles, and the second consists of rectangular 330x100nm nanoparticles. In both samples the horizontal gap Gap_H between particles was constant (~ 150 nm) while in vertical direction the gap Gap_V varied from 100nm to 400nm. The experimental and simulation results are presented on Figure 9a. As it can be seen from the graph the coupling strength is different for rectangular particles (expressed in overall resonance shift of 270nm) and square particles (expressed in overall resonance shift of 120nm). For elongated particles the coupling is much stronger, thus in order to reduce the interparticle influence in Y direction the gap should be at least 300nm. Such coupling should be taken into account in order to design broadband filter shape centered on the desired wavelength, otherwise strong interaction between unit cells will shift the unit cell resonance by hundreds nanometers. Experimental results of two additional three-particle-based metamaterials exemplify such intercell coupling influence (Figure 9b). In the first metamaterial the unit cells are separated by 300nm in vertical Y direction while in the second metamaterial they separated by smaller gap of 150nm. Metamaterial with large gap gives desired wide resonance around central wavelength 1300nm and presents a case of almost uncoupled unit cells – resonance of the whole metamaterial is similar to response of the single unit cell. But for metamaterial with smaller gap it is not a case. Although gaps that bigger than 100nm are generally treated as large and safe to eliminate interparticle coupling, we see that for elongated particples it is not a case and even for separation of 150nm the resonance is blue-shifted by more than 100nm from the desired resonance at 1300nm.

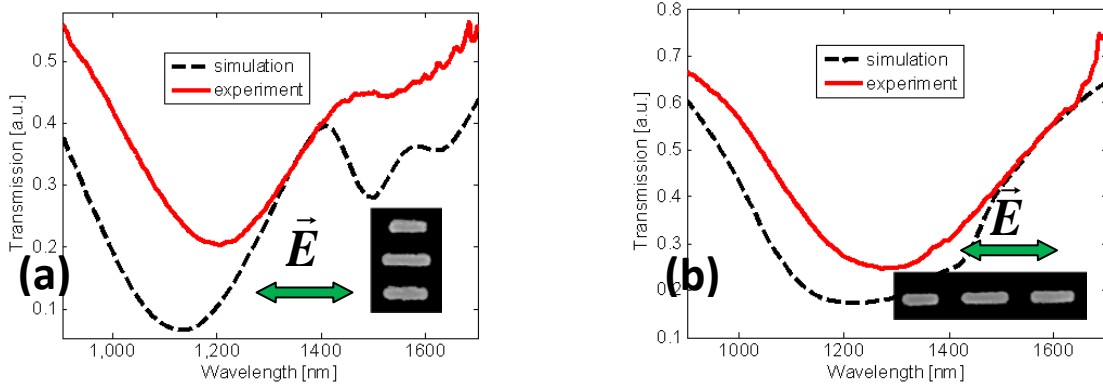


Figure 7. Simulation (black dashed line) and experimental (red solid line) spectra of the three-particle-based metamaterial: (a) parallel configuration and (b) serial configuration. Insets show SEM images of the related unit cells.

In summary we presented design rules for building the broadband metamaterials for NIR regime. We showed that serial combination of the nanoparticles has clear advantage for broadband applications since it makes impossible the excitation of out-of-phase modes for far-field excitation. Spectral dependence of metamaterials on separating gap between particles was shown experimentally and by FDTD simulations. Additionally it was demonstrated that elongated nanoparticles exhibit long-range dipole interaction, thus in order to eliminate coupling between such particles interparticle distance should be much bigger than in the case of point dipoles or square particles.

We acknowledge the partial support by AFOSR and the Israeli Ministry of Defense.

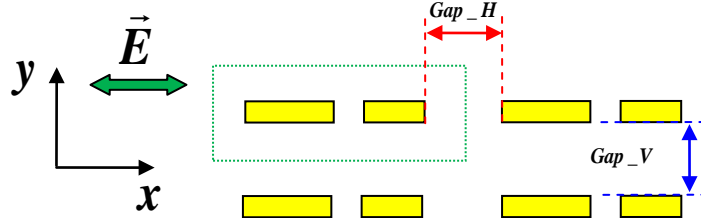


Figure 8. Scheme of the metamaterial in serial configuration

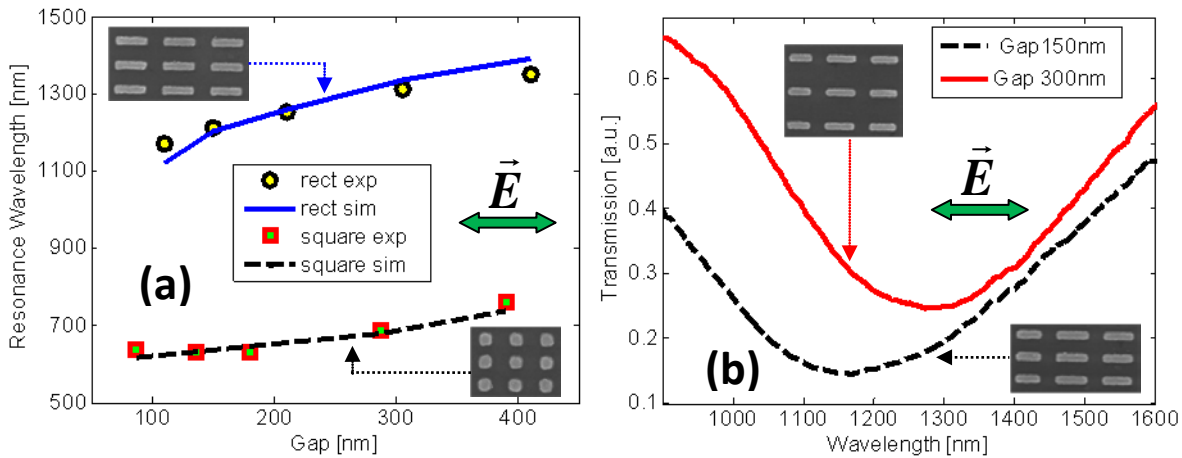
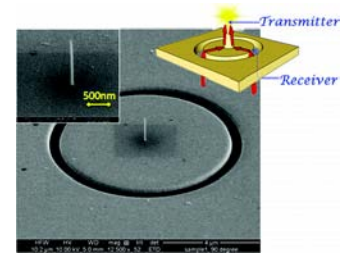


Figure 9. (a) Experimental and simulation of vertical gap dependence on the coupling between rectangular and square nanoparticles. (b) Experimental spectra of the three-particle-based metamaterials with vertical gaps 150nm and 300nm. Insets SEM images of the related samples.

- v. Light focusing by a tandem plasmonic antenna: tandem receiving-transmitting nano-antennas published in *Nanoletters* 11 pp 220-224 (2011)



There is an increasing interest in the manipulation of light-matter interaction on the nano-scale, promising a large variety of applications. The significant progress in this field is enabled by the fast development in nanometer processing techniques, such as electron-beam and ion-beam lithography, allowing fabrication of high quality metal nano-structures.

In order to cause an efficient interaction with light on the nano-scale, one has to confine the electromagnetic field much beyond its free-space wavelength. While conventional dielectric structures are incapable of supporting optical fields much below a half-wavelength cube volume, metallic structures at visible and near infra-red (NIR) regimes, having negative electrical-permittivity, do not exhibit such a limitation. Several configurations of plasmon focusing in two-dimensions were demonstrated – by carefully organized particles on a surface, by spatial gratings, or by circular grooves within metal films, preferably excited by radially polarized light. Here we demonstrate a plasmonic antenna that collects light from free space to be focused and captured in its near field, where an object of interest may be located. In our case another nano-antenna, a wire which is a part of a transmitting antenna, is the object of interest. While a related configuration was recently examined theoretically in the context of near field enhancement, here we perform scattering experiments (far-field measurements) to study the efficiency and coupling of resonances in the combined antenna structure. The structure is comprised of a receiving focusing plasmonic antenna (ring shaped), that converts the incoming beam to focused cylindrical plasmons on the rear side, which are subsequently coupled to a short vertical wire that assists in retransmitting to the far field (Fig. 1).

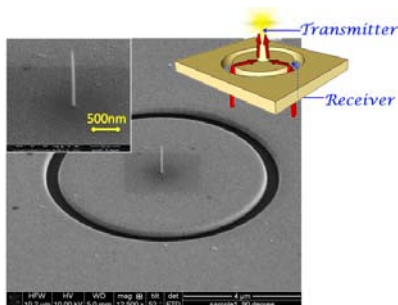


Figure 1. Experimental Sample – plasmonic wire grown at the center of the etched circular slit. Right inset – zoom on the wire region. Left inset – scheme of coupled antennas configuration

The devices were fabricated by a two-step process at the same chamber. First, the circular ring was etched using Focused Ion Beam (FIB) with a precise control over its dimensions. Subsequently, gold wires of different sizes were grown on the center of the ring by means of low current electron beam assisted local deposition of Au from gas phase precursor. The deposition of Au by this process always results in some carbon contamination (usually substantial) that modifies the optical property of the Au wire, mainly reducing its high negative dielectric constant. Thus an Energy-dispersive X-ray spectroscopy (EDX) was performed to the Au wire, (Fig.2)

confirming that a large percentage of carbon is diluting the deposited Au. These quantitative results were used to predict the actual permittivity of the wire.

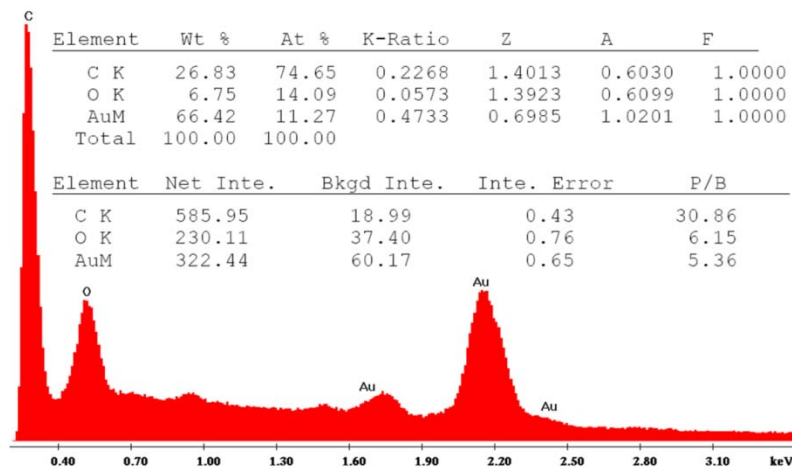


Figure 2. Material composition of the deposited wire, measured by EDX spectroscopy

Transmission spectra of the samples were measured using a tunable NIR laser (1510nm-1630nm) having a radial polarization (radial polarizer was implemented by sub-wavelength grating on silicon). The radially polarized light was focused by a microscope objective on the center of the plasmonic receiving annular antenna via the glass substrate (Fig.3), and was collected on the output port by another high numerical aperture objective. The input light was chopped and the output was detected by a large-area InGaAs detector, engaged in a lock-in scheme (Fig. 3). An IR-camera image of the transmitting antenna plane is shown in the inset, exhibiting the central hotspot.

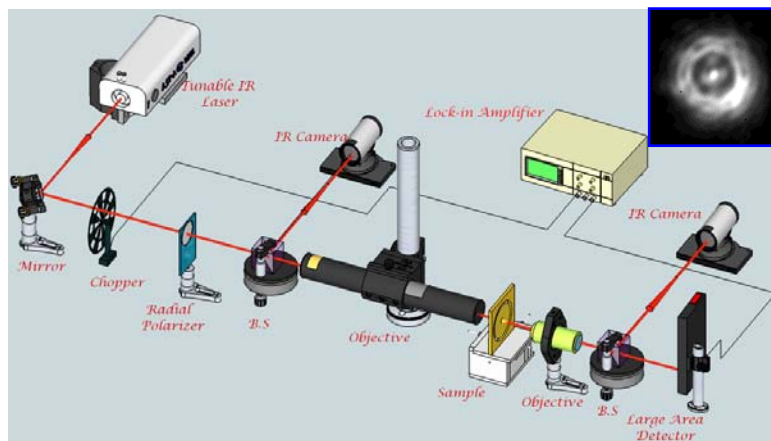


Figure 3. Measurement setup. A tunable NIR laser is radially polarized before impinging on the sample. Reflection path verifies 'center of the beam on center of the sample' alignment. The transmitted light is collected and detected by a large-area InGaAs detector in a lock-in scheme. Inset – IR-camera image of "long" antenna sample focused at antenna plane

The first set of experiments was performed when the plasmonic wire is embedded in air and the spectral transmission results are depicted in Fig. 4. The transmission spectrum for the same receiving configuration and varying the wire antenna dimensions was normalized by the spectral transmission of the ring antenna - which assisted also in elimination of the spectral response of the measurement system. The most significant signature in the transmission spectrum was recorded for the longest antenna – showing ~ 30% enhancement, indicating three orders of magnitude enhancement of the wire antenna cross section, estimated by the ratio of geometrical dimensions of the receiver ring and the wire as a stand-alone antenna. This effective cross section enhancement is of the same order of magnitude as for rigorously

calculated "particle above a surface" structures and exceeds significantly experimental results reported on single particles. Since the resonance of the wire should be dependent on the embedding media, a second set of similar experiments were performed with the same devices after embedding the wire (the whole transmission region) in PMMA. The transmission peaks were blue-shifted (Fig. 5) (as predicted by simulations) and similar values of ~30% peak transmission enhancement observed.

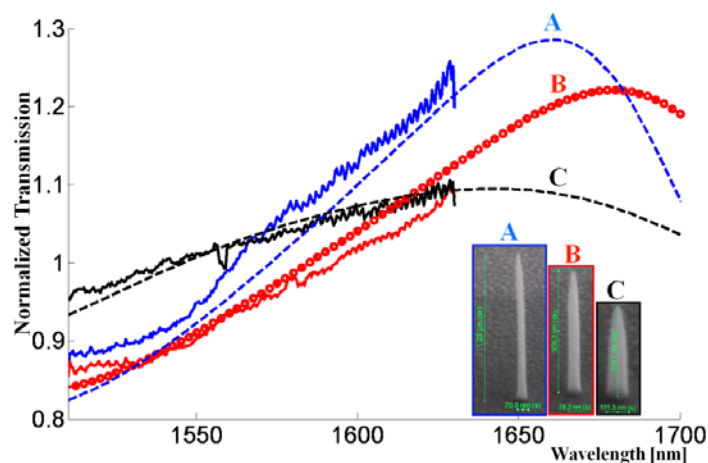


Figure 4. Transmission enhancement of the samples with wires, transmitter side in air, normalized by the ring antenna transmission. Measurement and theoretical fit of: long wire - solid blue line and dashed blue line, medium wire - solid red and red circles, short wire - solid black and dashed-dotted black

The Finite Element Method (FEM) was used to comprehend the measured data and to fit it with the theoretical predictions. Circular symmetry of the structure was exploited for reduction of the computation complexity, allowing denser grid and enhanced accuracy. The dielectric property of the antennas was adjusted according to the dilution values of the Au by carbon as extracted from the X-rays spectroscopic data and by employing the effective index model. The best fit was achieved for $\epsilon \sim -18+2j$. Total transmitted power was evaluated by integration of the far field power over the relevant boundaries and presented as a function of the wavelength. The normalization was performed as it was done for the experimental data. A good fit to all sets of measurements was obtained by the model. The simulated spectral peaks for the dielectrically embedded wire antenna, although located at the same wavelengths as recorded in the experiments are narrower for the simulation, probably due to additional inhomogeneity and scattering in the realistic dielectric coating. The transmission peaks correspond to the first Fabry-Perot resonance of the plasmonic wire antenna that was recently calculated.

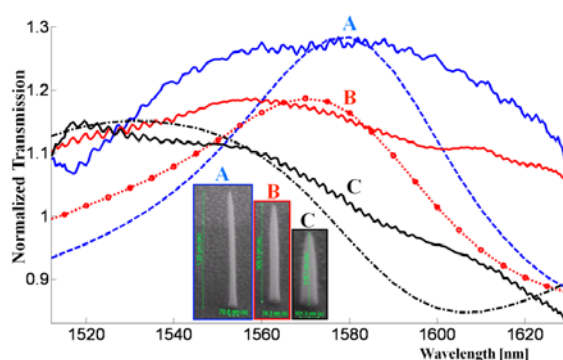


Figure 5. Transmission enhancement of the samples with wires, transmitter side covered by PMMA, normalized by the ring antenna transmission. Measurement and theoretical fit of: long wire - solid blue line and dashed blue line, medium wire - solid red and red circles, short wire - solid black and dashed-dotted black

A third set of experiments was performed to emphasize the unique role of the wire as part of the transmitting antenna. When the excitation direction was flipped – the wire antenna became a part of the receiving antenna, in contrary to the previous

experiments. The normalized transmission was measured again and compared to the previous results in Fig. 6, showing that when the wire is engaged within the receiving focusing antenna its contribution to the reception is minimal. This nonsymmetrical operation may be explained by the following: the regular excitation (top-left inset of Fig. 6) creates SPP within the circular slit, which were efficiently converted to rear-side in-plane surface waves by a 90° coupling. These SPPs converge to the center and excite the wire. On resonance, the wire is becoming an effective secondary source which reemits diverging plasmonic waves - the latter are partially radiated from the annular slit, thus contributing additional portion from the near field to the far field. It can be seen from the power distributions and their difference plots in Fig. 7 that the extra power is not radiated directly from the wire, but rather from the ring, preserving the same radiation pattern but with enhanced efficiency. On the other hand, in the flipped excitation (bottom-right inset of Fig. 6), the wire antenna in the center of the input donut-shaped radially polarized beam has an insignificant interaction with the impinging field, thus not changing the overall transmittance of the ring shape antenna.

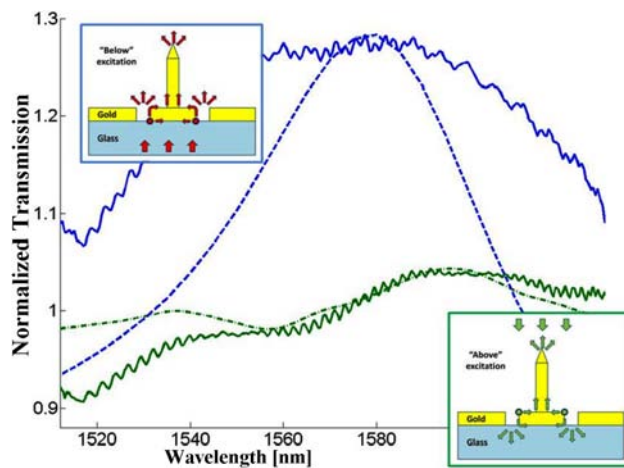


Figure 6. Transmission enhancement of the long wire sample of Fig. 5. Measurement (solid) and theoretical fit (dashed) of: excited from the receiving side – ‘below’ (as in Fig. 5) - green line, excited from transmitting side - ‘above’. Insets – schemes of ‘below’ and ‘above’ scenarios

In conclusion, we showed the response of a tandem plasmonic nano antenna assembly by measurements of the far field spectral response of the coupled structure. Although having a very small nominal aperture, the plasmonic wire has a significant signature and enhancement in the far field, which amounts to almost 3 orders of magnitude of cross-section enhancement. The results are in good agreement with FEM numerical experiment, with a reduced value of Au permittivity due to carbon dilution.

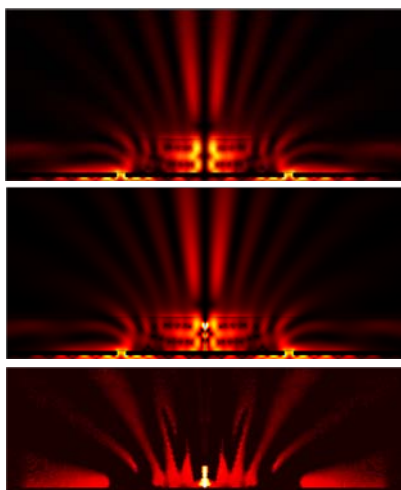
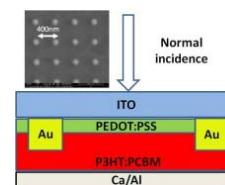


Figure 7. FEM simulation of power flow for the sample with the long wire of Fig. 5, at the wire resonance wavelength of 1580nm (a) – annular receiving transmitting antennas, (b) adding the central wire, (c) distribution of the power difference, zooming on the central area.

3. Antenna arrays in semiconductor devices

- i. Organic Solar Cell enhanced by antenna array
published in *Opt. Express* 19, A64 (2011)



1. Introduction

Organic photovoltaic devices (OPV), especially bulk hetero-junction (BHJ) cells, have gained much attention due to their potential for low-cost and high throughput production. However, the efficiency of OPV cells is still low, up to 5-6%. In order to achieve high efficiencies the device is kept very thin to reduce recombination losses, but must be optically thick to absorb most of the incoming light. Several methods have been suggested to overcome this limitation: tandem cells, folded structures, and new active materials.

An alternative approach is the exploitation of localized plasmon resonance of metallic nano-particle (MNP) arrays. Utilizing MNP to increase solar cell efficiency has been demonstrated in various thin film technologies and in silicon. In organic cells an increase in photocurrent was exhibited by incorporating either a solution of randomly distributed small MNP in the buffer layer of P3HT:PCBM cells, or as a thin layer of Ag in the buffer layer – or as a replacement of the ITO electrode by perforated Ag layer. Colloidal metal particles were reported also inside the active layer of a MEH-PPV:PCBM cell. However, while in inorganic cells good correlation between experimental results and theoretical-simulation models has been shown, investigations in OPV cells typically involve randomly distributed particles with size typically below 30nm which also exhibit random clustering rates, making it difficult to trace and optimize enhancement mechanisms using appropriate simulation models. The employment of small particles presents an additional drawback: allowing maximum resonance wavelength of ~450nm and relatively large absorption in the metal. The benefit of using larger sized silver prisms was recently shown using photo-induced absorption spectroscopy. In order to maximize the effect of the MNP on the cell efficiency, tuning the properties of the plasmon resonances and interactions is desirable. Thus the strategy of our study is based on a precisely controlled fabrication method using electron beam lithography (EBL) enabling a tight control of MNP array parameters such as particle size, shape, aspect ratio, and array period, all are affecting the resonance properties, allowing us to study the enhancement mechanisms and develop design guidelines. Upon success, mass fabrication techniques such as nano-imprinting can be used for commercial cell fabrication. Nanoimprint lithography – based on stamps prepared by EBL, preserves the fine accuracy of EBL, but can be used by a step and repeat procedure to cover the large areas of solar cells – in a massive, cheap and high throughput process. As a first step, 3D Finite difference time domain (FDTD) simulations of the entire cell were performed (discussed later) to analyze and optimize the MNP array parameters; subsequently the optimized parameters were implemented experimentally with good correlation to the predicted performance. A schematic illustration of the typical cell is shown in Fig 1.

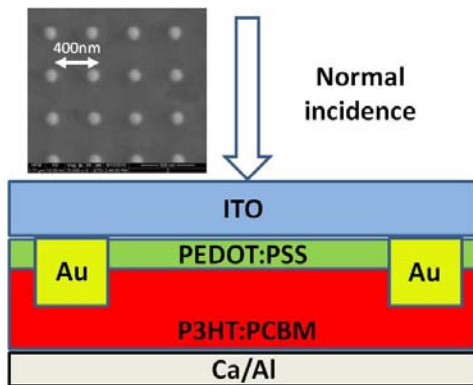


Figure.1 Schematic illustration of the device structure; (inset) SEM image of the fabricated MNPs array

2. Sample fabrication

The fabrication of the solar cell starts by patterning the Au nano particle array on the front electrode of the device. The array is produced on a glass substrate covered with a 100nm indium tin-oxide (ITO) layer by lift-off technique, employing EBL patterning (Raith E-Line). The EBL was performed by exposing PMMA layer using with a pattern of an array of circles. Subsequently a Au layer was deposited and then lift-off procedure – using acetone, took place to leave array of Au/Cr disks with height of 100nm, a diameter of 100nm (with variance of ~10nm) and center to center separation of 400nm. The inset of Fig 1 displays a SEM image of the resulting MNP array. A solution of PEDOT: PSS (poly(3,4-ethylenedioxythiophene) :poly(styrene sulfonate)) is then spin coated and dried at 110°C to form a 50nm buffer layer partially covering the Au particles. Subsequently a 1:1 solution of P3HT (poly(3-hexylthiophene)) and PCBM ([6,6]-phenyl C61-butyric acid methyl ester) is spin coated to form a 170nm active layer. Finally, Calcium (10nm) and Aluminum (120nm) are thermally evaporated using a contact mask.

The MNP array parameters were carefully chosen according to simulation results, as will be further discussed, such that the peak of the plasmon resonance is located at wavelength close to the P3HT:PCBM band-gap where it is less absorbing . The MNP height was chosen such that the particles will significantly protrude into the active layer to maximize the field enhancement effect. The array period is a tradeoff between minimizing metal absorption at shorter wavelength and increasing plasmon resonance strength. A detailed examination of the influence of each MNP array's parameter is discussed in the followings.

3. Results and discussion

The experimental results are summarized in Fig. 2, and the analysis of the measured features and their correspondence to theory, are shown in Figs 3-7.

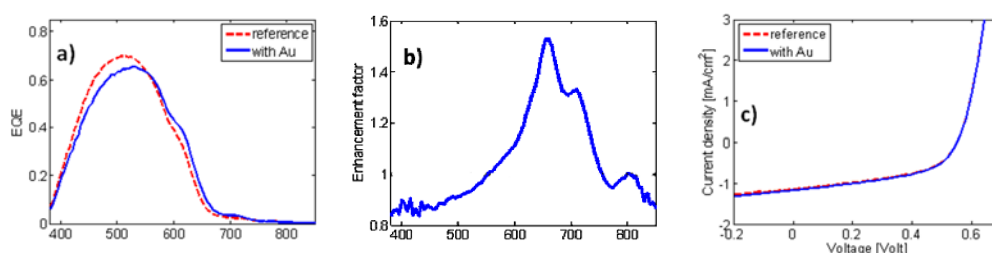


Fig.2 Experimental results of cell with Au MNPs array vs. reference cell. (a) EQE measurement. (b) EQE enhancement factor. (c) J-V characteristics.

Fig 2a shows the measured external quantum efficiency (EQE) of the cell with the Au MNP array compared to that of a reference cell. The cell under study and reference cell are located only few hundred microns apart to rule out variations due to slightly different processing of the organic material. Examining the enhancement ratio - Fig2b, a wide enhancement peak is observed for wavelength between 550-750nm with a major peak of 53% enhancement at 660nm and a minor peak of 33% at 710nm. Another small peak is registered between 780-820nm. An average reduction of ~10% in efficiency is observed at wavelength below 550nm. In Fig. 2c we depict the J-V characteristics, measured under 100 mW/cm² illumination by a solar simulator with an AM 1.5G filter, of the cell with the Au nano particles compared to a reference cell without. An increase of ~3.5% in short circuit current is observed, while open circuit voltage is unchanged.

To better understand the nature of the enhancement mechanisms we performed a FDTD simulation using Lumerical software for a cell of the same layer structure as the experimental one. The MNP array was modeled by Au cylindrical particles with height of 100nm and radius of 50nm embedded in the PEDOT:PSS and P3HT:PCBM layers with an array period of 400nm. A square unit cell and periodic boundary conditions with a normal incidence plane wave excitation from the ITO side was used. The dielectric functions for the different constituents were taken from the literature. The calculation mesh resolution was 5nm and it was verified that mesh of 2nms gave the same results, while the time step was 0.1fsec to assure convergence. The input plane wave was a short pulse (2.65fsec) to cover simultaneously all the range of the sun spectrum.

Figs 3a shows the fraction of power absorbed in the active P3HT:PCBM layer and in the metal for the cell with the MNP compared to the power absorbed in the active layer of a reference cell. The absorbed power at each wavelength is calculated in a standard procedure – by integrating the (light intensity (E^2) multiplied by the effective conductivity of the absorber) over its volume. Although the exact field distribution may be not so accurate due to the lack of knowledge of the exact nature of the interfaces, the absorbed power – as an integral measure is highly accurate. The extracted spectral enhancement factor is depicted in Fig 3b, exhibiting two enhanced absorption peaks at 680nm and 785nm while a reduction of ~10% in absorption is seen at shorter wavelengths. Clearly there is a very good correlation both in the enhancement peaks locations between simulation and measurement results, with the peak-width in the measurements slightly wider due to manufacturing inhomogeneity. The ~10% efficiency reduction at shorter wavelength also correlates well with the experimental results. The difference in enhancement magnitudes between simulations and the experiments as well as additional details such as the splitting of the main experimentally observed peak will be discussed later.

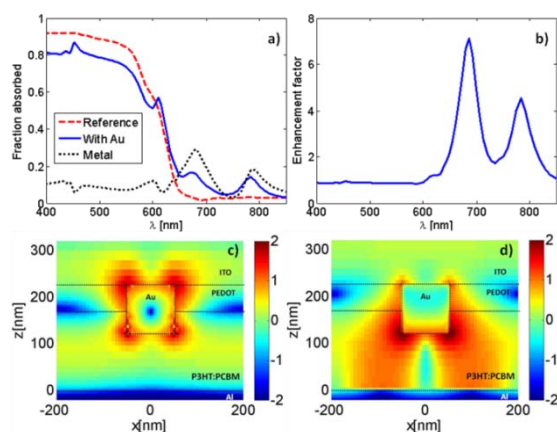


Fig.3 (a) Calculated (FDTD) fraction of power absorbed in the active P3HT:PCBM layer of a cell with Au MNPs compared to a reference cell. Fraction of light absorbed in the Au MNPs is also plotted. (b) Absorption enhancement factor. (c-d) Cross sections of electric field intensity normalized to incident source - log scale, at the symmetry axis $y=0$. (c) Plasmon resonance $\lambda=680$ nm (d) Patch antenna resonance $\lambda=785$ nm.

To further understand the enhancement mechanisms we examine the electric field intensity distribution at the two absorption enhancement peaks at 680nm and 785nm – Figs. 3c and 3d respectively. The resonance at 680nm exhibits a very strong local field enhancement in the vicinity of the particle, typical of the quadruple plasmon resonance, with lobes both in the PEDOT:PSS and P3HT:PCBM leading to enhanced absorption. The field penetrating into the metal results in undesired metal absorption, as seen in Fig 3a, however, this loss is minimized by using larger particles which have a higher scattering vs. absorption cross section. It should be noted that such larger particles with regular spacing can be easily fabricated by nano lithography patterning but are difficult to achieve when deposited from stable liquid dispersion – that was used in previous studies. The resonance at $\lambda=785\text{nm}$, Fig 3d, has a different origin. The electric field intensity distribution indicates that this resonance mode is the TM₁₁₀ mode of a circular nano-patch cavity generated between the Au nanodisk and the Aluminum back contact. This low radiation-Q optical antenna mode is beneficial for solar cell application – the energy is trapped mainly in the P3HT:PCBM layer leading to enhanced absorption in the active layer with less metal loss compared to the plasmon resonance mode case. Similar resonance was observed in OPV cells with a gratings based Ag anode. The patch resonance wavelength can be controlled by changing cavity height (i.e active layer thickness, or particle height) or size (particle diameter). The periodicity of the nano patch antenna array should be approximately a multiple of half the desired resonance wavelength ($\sim 390\text{nm}$) to avoid destructive interference, thus the structure acts at this resonance as diffraction gratings coupled with patch antenna array (also discussion related to Fig. 4 below).

Now we look into optimizing the plasmonic particles density (fill factor). The efficiency reduction at short wavelength, evident both in experiment and simulation results (Figs. 2 & 3), is caused by the Au particles, absorbing and backscattering some of the light. This phenomenon may look as posing an inherent tradeoff when determining the optimal density (or array period) of the MNP: lower MNP density will show less loss at shorter wavelength, but also reduced efficiency enhancement at the plasmon resonances. However, here the antenna effect of the plasmonic nano particles comes about to resolve this conflict. The influence of MNP density on the fraction of power absorbed in the cell is shown in Fig. 4. Decreasing MNP area density from 20% to 10% to 5% (array periods of 200nm, 280nm, 400nm respectively) decreases the short wavelength loss linearly, while the enhanced cell absorbance in plasmon resonance wavelength (660-720nm) is only slightly affected (the excursions of the resonance shape and splitting as a function of periodicity will be resolved in connection with Fig. 7). Only when increasing the period to 450nm (density $\sim 4\%$) the absorbance at plasmon resonance wavelength starts to decrease. The cause for this interesting phenomenon is the fact that at the plasmon resonance the effective particle cross section is much larger than its geometrical cross section, yielding a much larger effective density, while away from this resonance the cross section is the actual particle size. The desired particle density should be roughly inversely proportional to the effective particle cross section at the plasmon resonance, yielding both maximum absorption enhancement at plasmon resonance wavelength and minimum reduction outside the resonance. The dependence of patch resonance on periodicity discussed above is also evident in Fig 4 where the patch cavity resonance is exhibited only for periods of 400-450nm (densities of 4-5%).

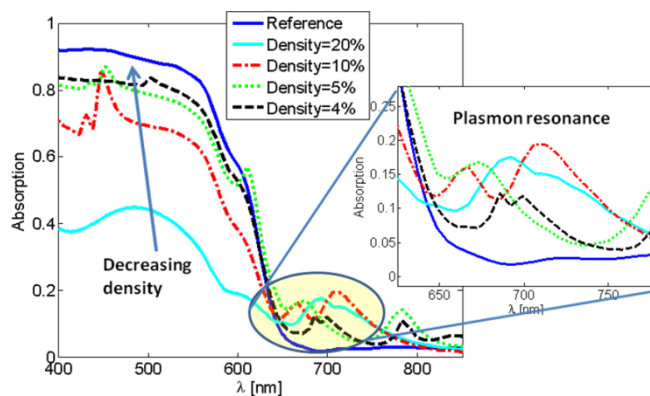


Fig.4 Calculated (FDTD) fraction of power absorbed in the photoactive layer of a cell with Au MNPs height of 100nm, radius of 50nm and varying density compared to a reference cell. (20% -period 200nm, 10% - period -280nm, 5% - period 400nm, 4% - period 450nm).

At this stage, and using Figs. 5 and 6, we look into the influence of the proximity of the metal structure to the active layer and also interpret by this effect the reduced experimental enhancement compared to the ideal simulations. First, we analyze a cell with shorter particles (height of 60nm), such that they are only slightly protruding the active layer. Absorption enhancement in the cell with the shorter particles is significantly reduced compared to the taller 100nm particles – Fig 5a. The electric field intensity cross section at the resonance for particle height of 60nm – Fig 5b, shows increased intensity mainly in the PEDOT:PSS and ITO layers, thus not contributing to enhanced absorption, leading to the conclusion that particles significantly embedded in the active layer are the better design choice. The small blue shift in the resonance stems from a decrease in the effective refractive index of the dielectric medium embedding the particle, now closer to the smaller PEDOT index (~ 1.45) than the higher P3HT:PCBM index (~ 2.1).

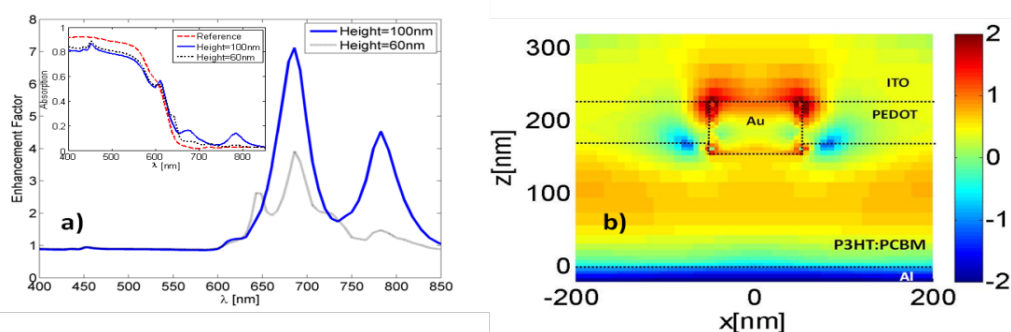


Fig.5 (a) Calculated (FDTD) absorption enhancement factor for cells with Au MNPs - heights of 100nm and 60nm compared to a reference cell (particle radius is 50nm and period 400nm). Inset - fraction of power absorbed in the active layer. (b) Cross section of electric field intensity normalized to incident source log scale, at symmetry axis $y=0$ - at the plasmon resonance $\lambda=645$ nm for particle height of 60nm.

Similar effect - remoteness of the metal particle from the active layer can explain the lower enhancement value in measurements compared to simulations. Although partially attributed to the inhomogeneity in manufacturing [28], most plausibly the dominant effect is that during the spin coating of the 50nm PEDOT buffer a residual very thin layer coated also the top 50nm part of the Au disks extending above this layer. This residual coating is reducing the absorption enhancement in the active layer, as verified by the simulation of such structure shown in Fig 6. It should be noted that this thin PEDOT coating of the Au particles may also have a positive effect

– eliminating the direct interface of the metal with the active layer thus decreasing the quenching of excitons in such metal-polymer interface, an effect not accounted for in our simulations.

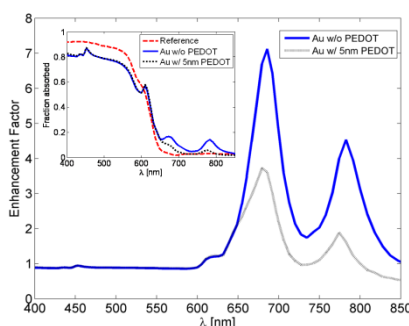


Fig.6 Calculated (FDTD) absorption enhancement factor for cells with Au MNPs: in direct contact with the photoactive layer; 5nm PEDOT layer buffering between the Au nanodisk and the active layer (In both particle radius is 50nm, height 100nm and period 400nm). Inset: fraction of power absorbed in the active P3HT:PCBM layer.

Finally, we are ready to interpret the last detail in the experimental result, namely the split at the main plasmon resonance (650-730nm, Fig. 2b), which is absent in the simulation (Fig. 3b). Similar split, with one major peak and a smaller peak at longer wavelength, is regained in simulation for slightly different periodicity of 350nm (Fig 7a). This split can be retraced to two interacting resonances: the highly localized quadrupole resonance exhibiting the larger peak at 665nm, Fig 7b, and a second, with smaller enhancement, peak at 695nm, Fig 7c. The second resonance is less localized and is similar to the patch cavity mode, but at this wavelength it is generated between the plasmonic particle and the top surface. Such resonance is thus sensitive to periodicity, as discussed previously in relation to the nano-patch mode which explains the dependence of this resonance shape as a function of the array density in Fig. 4. The slightly different periodicity between the simulation and experiment required to observe this split may be attributed to a difference in the simulated and actual permittivity of the active layer influencing the effective period. The third large peak at 745nm is again the patch antenna resonance discussed in connection with Fig. 3

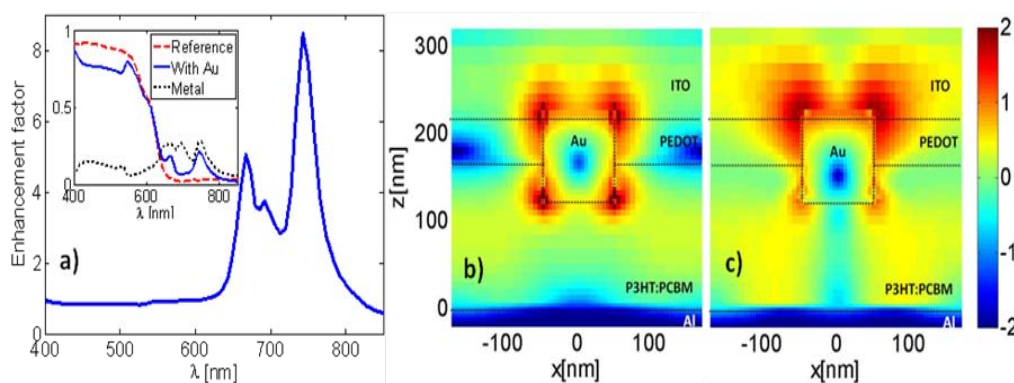


Fig.7 (a) Calculated (FDTD) absorption enhancement factor in a cell with Au MNPs compared to a reference cell. Au MNP height is 100nm, radius 50nm and period 350nm. Inset: fraction of power absorbed in the active layer and the absorption in the Au. (b-c) Cross sections of electric field intensity at the split peak of the plasmon resonance (log scale normalized to incident source), (b) Peak at $\lambda=665$ nm (c) Peak at $\lambda=695$ nm.

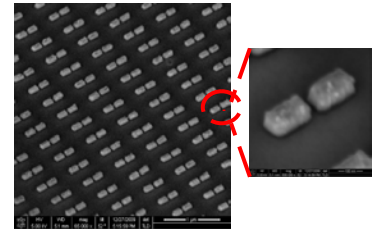
4. Conclusion

In conclusion, we have shown both experimentally and theoretically an increase in the EQE of OPV cells after embedding ordered arrays of Au NPs extending into the active layer. We identified two enhancement mechanisms, enhanced absorption

driven by local field enhancement of the plasmon resonance and enhanced absorption driven by a cavity mode of a circular nano patch antenna. Based on an analysis of these mechanisms we derived design guidelines for optimal MNP properties. Particles should protrude into the active layer in order to maximize the near field enhancement. Optimal particle density is roughly inversely proportional to particle cross section at the plasmon resonance leading to minimum absorption and reflection losses at wavelength outside the resonance. A thin coating layer around the Au particles causes some reduction in near field enhancement, but may also reduce exciton quenching at the metal polymer interface. It is important to remember that the polymerization of the photoactive layer itself can be modified by changing the interfaces – thus adding MNP may result in structural related spectral changes. However, due to the small fill factor (5%), the fact that the metal disks are covered by thin buffer layer even when they are residing in the active layer, the fact that the enhancement is obtained exactly at the calculated plasmon resonances (independent of the original spectrum as we obtained by measurements of a different photoactive blend-not reported here), makes our interpretations highly plausible.

ii. Faster LED by antenna array: emission rate enhancement from InP MQW emitter

Published in *Opt. Ex.* 19, pp. 9807-9813 (2011)



1. Introduction

Integration of electronic and optical devices in the 100nm scale poses a challenge for optics, requiring sub-wavelength confinement, guiding, manipulation, emission and detection of light. A possible way to face this challenge is by using metal-dielectric plasmonic structures which offer sub-wavelength optical confinement, and are relatively easy to manufacture on glass or semiconductor in a fab-compatible environment. A nano-antenna is designed to effectively couple the electromagnetic field generated by an emitter located in its near-field, to the far-field wave that can be collected and further used. In addition, the high intensity of vacuum electric field confined at the vicinity of the nano-antenna modifies the density of states to which a close-by emitter can couple, therefore increasing the free space emission rate. Properly designed metallic nano-particles and structures, incorporating small size, sharp corner or narrow gap, have more significant local field enhancement, thus enhancing emission and absorption rates. On the other hand, larger size particles have greater scattering to extinction cross-section ratio and better coupling to the far-field. Nano-antenna design should maximize both characteristics.

Surface plasmon enhanced spontaneous emission was demonstrated in various systems: metal coated nanoshell, CdSe/ZnSe nanocrystals and InGaN single quantum well (QW) coupled to SPP waves propagating on a thin metal layer; Si-nanocrystals coupled to periodic metallic gratings; Si Quantum Dots (QD) embedded in silica, and fluorescent dye molecules coupled to localized plasmon fields of a single plasmon nano-antenna, or of an array of nano-antennas, and Er^{+3} emitters coupled to a quasi-periodic array. While previous experiments were performed mainly on discrete emitters such as molecules or quantum dots, on low index substrate, emitting at visible or near-visible IR wavelengths of 400 to 900nm, this work focuses on a continuous semiconductor gain medium, InP-based multi quantum well (MQW) structure operating at room-temperature and emitting in the telecom wavelength regime of $1.5\mu\text{m}$, coupled to an array of gold nano-antennas. Using a continuous MQW gain medium simplifies the sample manufacturing as no alignment of the emitter to the nano-antennas is required, moreover enhanced emission from a larger area can be accumulated.

We demonstrate enhancement of light emission from optically-pumped InP MQW using different arrays of gold single-strip and double-strip nano-antennas, selectively tuning the peak of enhanced emission according to nano-antenna resonance wavelength. Comparison to theoretical model shows that most of the enhancement is attributed to a reduction in the radiative recombination lifetime in the QW, which paves the way to the development of high-speed directly-modulated nano non-laser emitters.

2. Measurement results

Nano-antennas shape was chosen to be of short strip, and of two coupled short strips with a narrow gap in between, as elongated shape and high refractive index of our

semiconductor substrate red-shifts the resonance for polarization parallel to the long axis. The advantage of the double-strip structure is that the electric field is greatly enhanced in the narrow gap between the strips which enhances the emission rate, and the overall nano-antenna scattering cross-section is greater than a single-strip. An estimation of nano-antenna size resulted from a quasistatic analysis of a gold ellipsoid embedded in InP, yielding a resonance at 1500nm for a particle length of 250nm. Following FDTD simulations (using the Lumerical software package) with the parameters of the manufactured antenna: width of 100nm and thickness of 60nm, yielded more accurate resonance values of 1400nm (fig. 1a) and 1640nm for 200nm and 250nm long single-strip antennas respectively. Simulations of the double-strip antennas exhibited enhanced field in the gap (fig. 1d), and a spectrum showing a small 10nm red-shift for a gap size of 50nm (fig. 1b).

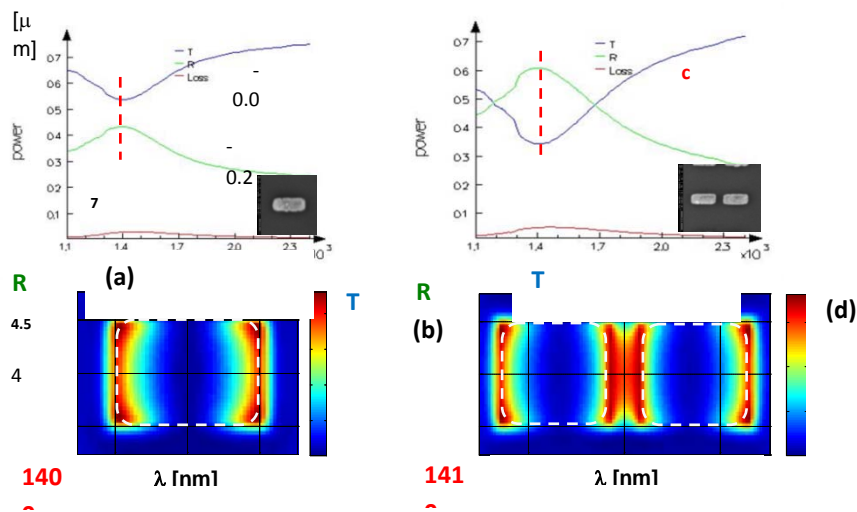


Fig. 1. FDTD Simulated transmission and reflection spectrum of (a) 200nm single-strip, and (b) 2x 200nm double-strip with 50nm gap, and (c,d) Electric field amplitude respectively.

The samples were grown by metal organic molecular beam epitaxy (MOMBE) on an InP substrate. The layer structure consisted of 4 InGaAs/InP 8nm/20nm QWs, with a 20nm intrinsic InP layer ending the QW stack (fig. 2a). Nano-antenna arrays were fabricated on top of the InP MQW stack by E-Beam Lithography, followed by evaporation of gold, and a subsequent lift-off process. Resulting nano-antennas dimensions were 60nm thick, ~100nm wide, lengths in the range 200-350nm, and gaps of 50 and 100nm for the double-strip antenna (fig. 2b-d). PL from the optically pumped sample by a 532nm laser showed strong emission with a peak at 1540nm.

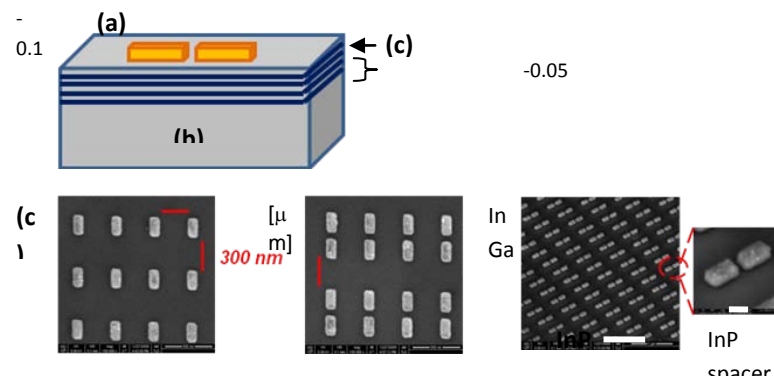


Fig. 2. (a) Schematic of the Au double-strip nano-antenna on InP sample. SEM images of the nano-antennas on InP MQW, (b) 200nm single-strip, and (c,d) 2x200nm double-strip.

Nano-antenna transmission spectrum measurements of the un-pumped nano-antennas, normalized to a reference having no nano-antennas, were performed using a white light source for both parallel and perpendicular polarizations relative to the long-axis of the antenna. Subsequently PL spectrum from the optically-pumped MQWs in the nano-antennas array region was measured, and normalized to the PL from a close region with no nano-antennas, resulting in the PL enhancement spectrum. Nano-antenna normalized transmission spectrum (fig. 3a,b, 4a,b), and respective PL and PL enhancement measurements (fig. 3c,d, 4c,d), are shown below for the single-strip and double-strip nano-antennas.

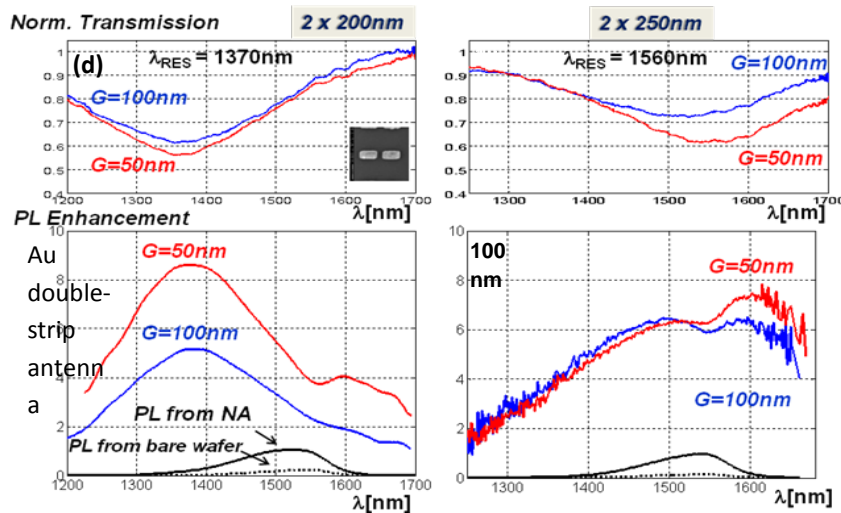


Fig. 3. (a,b) Normalized transmission spectrum of double-strip nano-antennas (a) 2x 200nm, (b) 2x250nm, with gap of 50nm (red line) and 100nm (blue line). (c,d) PL enhancement spectrum for respective nano-antennas (blue), emission from reference (dotted), and emission from nano-antenna region (full).

The nano-antennas measured resonance wavelengths were in good agreement with simulations results. PL enhancement of ~ 9 was measured for the 2x200nm double-strip antenna with 50nm gap (fig. 3c), at a wavelength of 1340nm, corresponding to the resonance wavelength of the nano-antenna of 1370nm (fig. 3a). The larger 100nm gap antenna gave a 'shallower' resonance and a smaller enhancement of ~ 5.2 . For the 2x250nm double-strip antenna with 50nm gap enhancement of ~ 7.5 was measured (fig. 3d), with shift in PL enhancement peak to ~ 1600 nm relative to the antenna resonance wavelength of 1560nm (fig. 3b). The single-strip nano-antenna gave maximum PL enhancement of ~ 5.2 (fig. 4c), again with peak enhancement corresponding to the nano-antenna resonance wavelength.

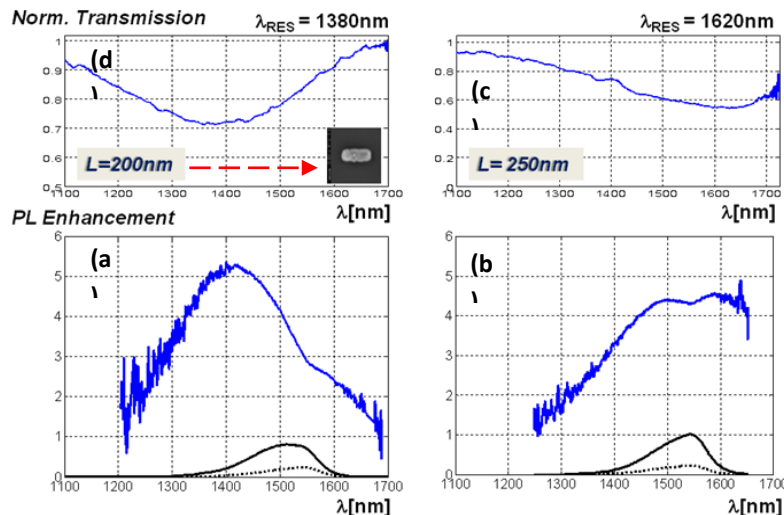


Fig. 4. (a,b) Normalized transmission spectrum of short-stripe nano-antennas (a) 200nm, (b) 250nm long. (c,d) PL enhancement spectrum (blue), emission from reference (dotted), and emission from nano-antenna region (full).

3. Theoretical modeling and simulation

We used the theoretical model presented by Sun et. al. [8] together with FDTD simulation results to interpret the experimental results and estimate the physical parameters involved. The plasmonic enhancement of the vacuum electric field by the nano-antenna modifies the density of states available for emission, thus increasing the radiative recombination time of the MQW by the Purcell-factor, $\tau_{rad}' = \tau_{rad}/F_P$, and enhancing the measured PL. For InGaAs/InP QW's at room temperature non-radiative recombination dominates, with $\tau_{nrad} \sim 1\text{ns}$ and $\tau_{rad}/\tau_{nrad} \sim 10$ (values depending on carrier concentration, and material and sample details), leading to a spontaneous radiative emission efficiency $\eta_{rad} = 1/(1 + \tau_{rad}/\tau_{nrad})$ of $\sim 9\%$ [25]. The emitter is coupled to the plasmon modes of the nano-antenna, which are then coupled to radiation modes with an efficiency η_{pr} . The overall radiative recombination efficiency in the presence of plasmon nano-antennas is given by [8]: $\eta_{sp} = \eta_{pr} \cdot \frac{F_P \tau_{rad}^{-1}}{F_P \tau_{rad}^{-1} + \tau_{nrad}^{-1}}$ and

the enhancement in the PL is given by the ratio η_{sp}/η_{rad} .

Part of the enhancement measured in the experiment comes from the angular gain of the nano-antenna, namely the narrowing of the native PL angular distribution due to the interaction with the nano-antenna [26], causing increased light collection by the limited numerical-aperture (0.85) of our objective lens. Without nano-antennas 3.5% of the uniformly distributed emitted light ($\eta_{ext} = (\text{N.A.}/n_{\text{InP}})^2/2$) is collected by the objective lens. FDTD simulations of the nano-antennas shows a narrower angular distribution, increasing the lens collection efficiency by a factor of $F_{\text{lens}}^{(D)} = 2.2$ for the double-strip nano-antenna, and $F_{\text{lens}}^{(S)} = 1.5$ for the single-strip. Correcting the maximum measured PL enhancement by this antenna-gain factor, results in radiative enhancement factor of 3.2 for the single-strip antenna, and of 4 for the double-strip antenna, which is 25% better than the single-strip.

PL can also be increased by resonant enhancement of the pump by the nano-antenna. However for these nano-antennas with resonances at 1360nm and 1540nm, no enhancement of the excitation at 532nm occurs.

The overall enhancement in measured PL, F_{PL} , is thus given by:

$$F_{PL} = F_{\text{lens}} \cdot \eta_{pr} \cdot \frac{1 + \tau_{rad}/\tau_{nrad}}{1 + (\tau_{rad}/\tau_{nrad})/F_P} \leq \eta_{pr} F_{\text{lens}} \cdot \frac{\tau_{rad}}{\tau_{nrad}} \quad (1)$$

where the limiting value is achieved for $F_P \gg \tau_{rad}/\tau_{nrad} \gg 1$.

Apparently a significant reduction in radiative recombination time requires a large Purcell-factor, which together with a large plasmon-to-radiation coupling efficiency will lead to large enhancement in measured PL. It can be deduced from equation (1) that for this system of InAsAs/InP MQWs the maximum attainable radiative enhancement factor is of the order of the original $\tau_{rad}/\tau_{nrad} \sim 10$, and that Purcell factors higher than 100 are not required.

We used FDTD simulation results to evaluate the Purcell factor in our experiment using the expression [15]: $F_P = \frac{3}{4\pi^2} \cdot \frac{Q}{V_{\text{eff}}/(\lambda/n)^3} \cdot \left(\frac{E}{E_{\text{max}}}\right)^2$, where the quality factor Q is

estimated from the PL spectrum to be $Q \sim 10$ for the short-stripe and ~ 12 for the

double-strip nano-antennas, V_{eff} the effective mode volume calculated from electromagnetic energy distribution around the nano-antenna: $V_{\text{eff}} = \iiint \left[\frac{d(\omega\epsilon)}{d\omega} |E|^2 + \mu_0 |H|^2 \right] dx dy dz / \max \left[\frac{d(\omega\epsilon)}{d\omega} |E|^2 + \mu_0 |H|^2 \right]$, and the electric field is averaged over the simulation unit cell at the planes of the QWs. The resulted Purcell factor values are: $F_{\text{P, Double}} \sim 25$ and $F_{\text{P, Single}} \sim 13$, where the higher Purcell value of the double-strip nano-antenna comes from the higher field confinement in the gap and a slightly longer penetration into the substrate. Using the model of equation (1), with $\tau_{\text{rad}}/\tau_{\text{nr}} = 10$, the calculated Purcell and lens collection factors, and with η_{pr} fitted to be ~ 0.5 , gives calculated PL enhancement values of 4.8 for the single-strip and 8.6 for the double-strip nano-antenna, in good agreement with the measured maximum PL enhancement values of 5 and 9 respectively. This implies that with the 2x200nm double-strip nano-antennas the radiative recombination time is shortened by a factor of $1/F_{\text{P}} \sim 1/25$ from $\sim 10\text{ns}$ to $\sim 0.4\text{ns}$, and that the overall recombination time reduced by a factor of $1/3$ from $\sim 0.9\text{ns}$ to $\sim 0.3\text{ns}$. The plasmonic nano-antennas increased the radiative recombination rate such that the overall recombination rate is governed by radiative rather than non-radiative recombination.

4. Summary

Gold single-strip and double-strip nano-antennas were fabricated over InP substrate containing MQW. The photo-luminescence from the MQWs was measured and shown to enhance by a maximum factor of 9 and 5 for the double and single strip nano-antennas, where maximum enhancement wavelength tunes in resonance with the nano-antennas. The plasmonic nano-antennas increase lens collection efficiency, and shorten the radiative recombination time of the excitons in the QWs by Purcell factors - calculated from FDTD simulations of 25 and 13 for the double and single strip nano-antennas respectively, resulting in the enhancement values obtained for the measured PL. This implies that the coupling to the double-strip nano-antennas reduces radiative recombination time of carriers in the QWs, making it shorter than non-radiative recombination time, and reducing overall recombination time by a factor of ~ 3 . Better designed nano-antennas, in closer proximity to the QWs, and gaps smaller than 20nm, will result in Purcell factors higher than 100, and in even shorter radiative recombination times. This can have greater impact than merely increasing PL efficiency – by substantiating a path for direct modulation of such LEDs in rates exceeding few Gb/sec, and thus enabling their use in optical short-reach data communications applications.

iii. Antenna metamaterial for current injection LEDs (ongoing work)

Plasmonic enhancement of emission was demonstrated; however it was accomplished by employing an optical pump. As an important step towards integration of this enhancement into a real device, electrically operated LED is studied consisting of well-designed and accurately fabricated nano-antennas - operating at room temperature. The main barriers are due to the fact that the active layer (quantum well or dots) should be very shallow – namely in the vicinity of the antenna plane. This is translated to a very thin doped semiconductor (p or n) above the emitting layer – which is problematic for current spreading. The main conclusion from this research is that in order to spread the current correctly – we should use the nanoantenna array itself as a contact layer. This necessitates the actual interconnection of all the antennas – which modifies substantially their plasmonic enhancement and resonances. This research results are providing solutions to the proper design of interconnected array of nanoantennas.

The following steps were performed: antenna array was designed to have a resonance at the same wavelength as the LED emission; The antenna array were in close proximity to the emitting layer of the LED; The device geometry is designed to allow injected carriers to reach hotspots of the nanoantennas area, causing the device size to be diffusion length limited, unless carriers can be injected from the nanoantennas.

A LED structure having InGaAs QW as the active material was grown on an n-type InP. The PL of the sample was measured and the PL matched the expected emission from InGaAs QW.

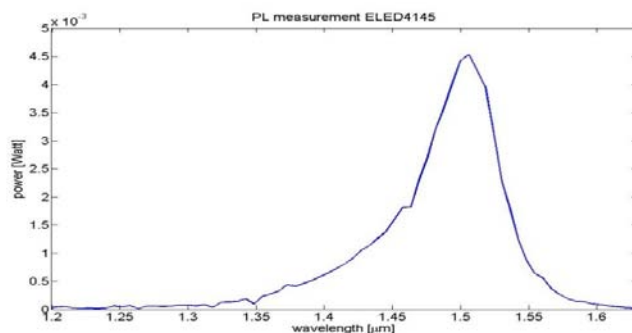


Figure 1: InGaAs QW PL measured spectrum.

The diffusion length was measured with optical pumping in order to know what should be the maximal size of the LED. Using a camera and by the light emitted from the QW (Figure 2) and calculate the carriers' diffusion length. It was found to be 17μm.

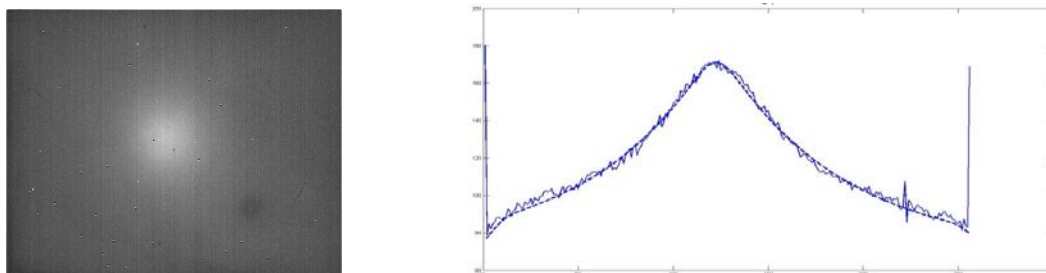


Figure 2 a) PL spot on camera; b) PL power as function of space along a cut through its maximum

Design of the Nano-Antennas was performed in order to get a resonance wavelength at the PL wavelength. Different shapes, sizes and materials were simulated looking for the highest field enhancement.

E-beam lithography of the nano-antennas and basic SEM and resonances measurement were done. Very good agreement between the actual structure and the designed structure was achieved, and the measured resonances fitted to the planned resonances.

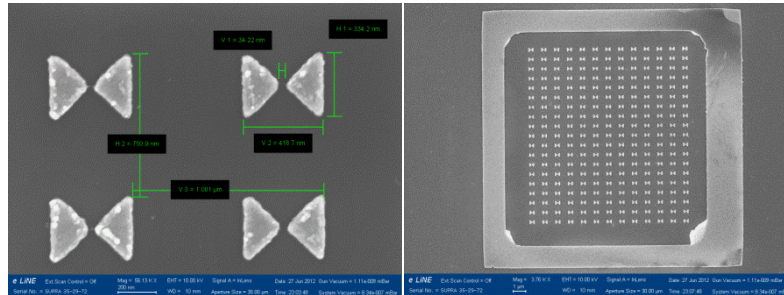


Figure 3: SEM pictures of bow-tie nano-antenna

The final LED structure with the contacts was prepared

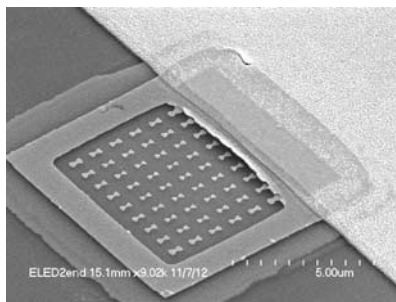


Figure 4: Schematic diagram of the LED device with contacts.

A reference (no antennas) sample was measured and the EL was found to be similar to the PL (Fig. 5a) and I-V curves were found to have good agreement with theory (Fig. 5b).

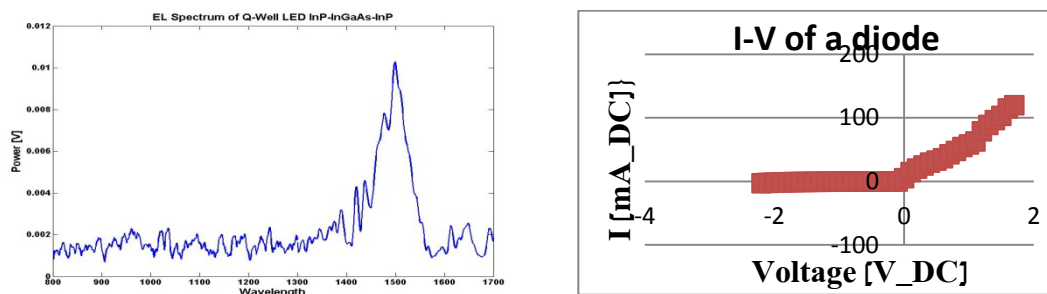


Figure 2: InGaAs QW LED a) measured EL spectrum; b) measured I-V curve

EL spectrum of the antenna enhanced LED sample together with IV curved was measured, and found to be similar to the reference sample, but with less intensity and small SNR. In addition, it was noticeable that the light emitted from the LEDs is coming mainly from the frame area, and not from the center area of the LED where the nanoantennas are located. After some consideration of the design it was found out that the diffusion length might have less influence under electrical field due to drift of the carriers. The conclusion is that the sheet resistance is larger than 2MΩ per

100um (length of the contact), and current spreading from the contacts to active area inside the 5nm N-type layer is inefficient and insufficient.

New Design Concepts for Electrical Pumping with Current Spreading

In order to overcome the current spreading issue we considered 3 methods: first - design current spreading contacts with a lengthwise and crosswise stripes along the LED, containing the nanoantennas in-between; use Indium-Tin-Oxide (ITO) as transparent contact covering the nanoantennas; and design current spreading contacts with lengthwise stripes along the LED connected directly to the nanoantennas.

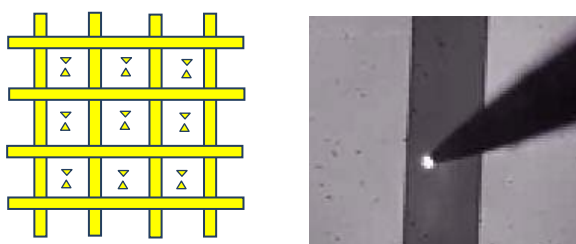


Figure 63: a) Criss-cross contacts for current spreading; b) LED under current injection with N-side ITO contact

Method 3 – the interconnected nanoantenna is innovative and requires novel design rules for the antenna. We used FDTD simulation to find out how the fact that nanoantenna is connected to a stripe is effecting its resonances and field enhancement. Simulation results are shown in Fig. 7. The colors indicate the field magnitude ($|E|^2$) inside the InGaAs QW and the dashed lines represent the Au interconnected nanoantennas above the QW. It was found that at resonance the magnitude of the fields is enhanced by factors of 30-40 which compared to separated nanoantennas (factors of about 50) is by 20% less, however with other advantages as mentioned.

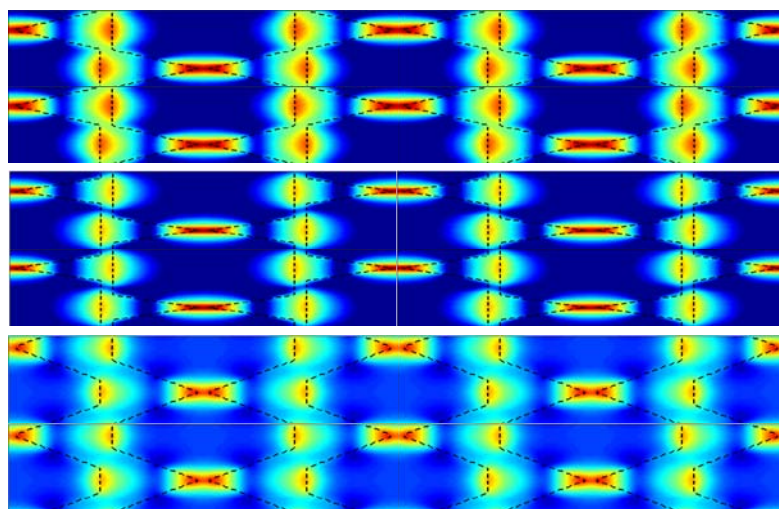


Figure 7: Connected bowtie nanoantennas with different base sizes: (a) small base; (b) medium base; (c) large base.

It was also found that the connecting stripe width strongly influence the enhancement, so that the wider strip has a smaller the enhancement.

This connected nanoantennas design was fabricated with improved layer design; p-type InP substrate, 50nm InP p-doped, 10nm InP intrinsic, 5nm InGaAs QW as active, 5nm InP intrinsic, 5nm InP n-doped, Ti/Au contacts.

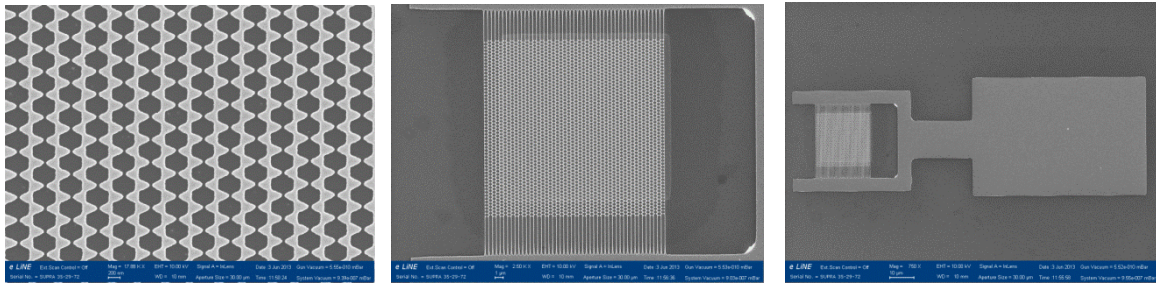


Figure 8: SEM of interconnected nanoantennas and the probes pad

Measurements of these LEDs are underway.

iv. Enhanced SWIR GaN quantum cascade detector

Abstract

We demonstrate a normal incident GaN/AlN alloyed quantum cascade detector (QCD) excited by surface plasmons resonance using an Au two-dimensional metal holes array integrated on top of the detector absorption region. The device photodetection peaked at 1.82 μm at room temperature. We show experimentally that a properly designed two dimensional metal hole array -CQD photodetector can facilitate a strong plasmonic-intersubband resonance interaction, leading to an absolute enhancement by factor 2.5 of infrared photoresponse in comparison with 45° polished edge coupling device. Our study indicates two key mechanisms for the performance improvement. One is the TM localized nature of the plasmon polariton surface wave that permits an efficient coupling to the normal incident far-field light. The other is an absolute enhancement by one order of magnitude of the absorption cross section per quantum well due to the strong near-field optical intensity. The results of this work demonstrate that the metal hole array technology can bring a substantial improvement to the responsivity of GaN based alloy QCD device while allowing normal incidence illumination.

Introduction

Quantum cascade detectors (QCDs) are an appealing alternative to quantum well (QW) infrared photoconductors because these photovoltaic devices operate at zero bias, and therefore do not suffer from dark current [1]. Thanks to the large conduction band offset offered by the GaN/Al(Ga)N material system, III-nitride based QCDs allow to reach near-infrared wavelengths as short as 1 μm . However, according to the polarization selection rule of intersubband transitions, infrared absorption is possible only when the electric field vector of the radiation has a component perpendicular to the quantum well layers. For characterization, GaN QCDs are usually illuminated through a 45° wedge polished surface or at Brewster angle front illumination, resulting in part of the electric field normal to the QWs. Yet for most technical applications, as mentioned above, planar device geometry and large area illuminating are essential.

Integrating a better light coupling in GaN-based QCD's is a key factor towards applicative implementations with large illuminated focal plane area at normal incidence and enhanced responsivity. Normal incidence can be achieved by processing a top grating on device surface. The function of the grating is to scatter radiation entering from the rear side of the wafer away from the direction normal to the surface, enabling inter-subband absorption. The responsivity enhancement of grating with respect to 45° angle wedge illumination is a factor of 2- to 3 depending on the grating coupling efficiency. In addition to simple light coupling scheme these devices use resonant absorption to improve the detector performance. An alternative technique demonstrated, involving V-grooves with nearly 45° slopes on the mesa facet. Enhanced performance demonstrated by recently using more complex structures like photonic crystal-QWIP and enhanced QWIP utilizing photonic crystal slab resonator.

A different new effective approach has emerged recently. It makes use of two dimensional metallic holes arrays (MHAs) and generation of surface plasmon waves (SPW). The SPW is bound to the metal/dielectric interface with an evanescent field that decays exponentially away from the interface. Resonances are observed when a wave vector of the array provides phase-matching between the incident photon and SPWs at either of the metal/dielectric interfaces. Surface plasmon supports TM mode and requires the electric field being normal to the surface because of the generation of surface charge. In addition, a carefully designed plasmonic array forms standing waves and produces a cavity effect, which leads to an enhanced transverse plasmonic mode. Therefore, if properly coupled, surface plasmons can resonate with electron ISB transitions, and efficiently excite carriers in the QWs to generate a strong photocurrent.

Most of recent, innovative approaches to enhance infrared absorption and improve infrared detector performance by sub-wavelength, MHAs were focused on quantum dot infrared photodetectors (QDIPs), where quantum dot electron confinement enables normal incidence absorption by modifying the optical transition selection rule in comparison to QWs. However, as far as we know, there are very few experimental studies that applying surface plasmons to enhance the sensitivity of quantum well infrared photodetector (QWIPs) or QCDs which are only sensitive to electromagnetic waves which have electric field component normal to the quantum well surface. More ever, today, there is no successes full experimental demonstration of an absolute enhancement of infrared absorption cross section arising from the SPP interaction with - ISBT in QWs or QDs, where all previous papers discussed the SPP effect on detector performance.

In this work we demonstrate that MHA technology provides a substantial improvement to the responsivity of GaN based alloy QCD device, while allowing normal incidence illumination – paving the way for pixelated imager based on such material. The principle of operation is to convert the incoming light into a TM-polarized surface plasmon wave (SPW), which excites the ISB absorption in the QCD device. In addition we demonstrate, experimentally, an absolute enhanced absorption cross-section per quantum well due near field optical intensity enhancement.

2. Design and device fabrication

Surface plasmons polariton (SP) are bound electromagnetic (EM) excitations propagating at an interface between a metal and a semiconductor. The origin of these surface waves is a coupling of EM fields to electron plasma of the conductor. For normal incident surface plasmon polaritons (SPP's) are characterized by the dispersion relation

$$(1) \quad |k_{SPP}| = \frac{\omega}{c} \sqrt{\frac{\epsilon_m \epsilon_d}{\epsilon_m + \epsilon_d}}$$

where k_{SPP} is the surface plasmon polariton wave vector, ω the optical frequency, c the speed of light and ϵ_d and ϵ_m the dielectric constants of the sample layer in contact with the metal and the metallic film on top of it, respectively. The SPW are generated at the interface between the illuminated MHA and the uppermost dielectric layer of

the QCD. The dispersion curve of surface plasmons lies below the light line separating free space photons from evanescent ones. In other words, the momentum of a surface plasmon is greater than momentum of a free space photon. Thus, it is not possible to directly couple light into plasmons propagating at a metal semiconductor interface. One way to provide the missing momentum \mathbf{G} necessary for coupling incoming light to SPP is to use periodic holes array. The interaction is made allowed by coupling through the grating momentum and obeys conservation of momentum $\mathbf{k}_{sp} = \mathbf{k}_x \pm i\mathbf{G}_x \pm j\mathbf{G}_y$ where \mathbf{k}_{sp} is the surface plasmon wave vector, $\mathbf{k}_x = (\omega/c)\sin\theta$ is the component of the incident light wave vector that lies in the plane of the sample where θ is the incident angle relative to surface normal. $|\mathbf{G}_{x,y}| = 2\pi/a_{x,y}$ are the reciprocal MHA lattice vectors with a lattice constants a_x and a_y , and i, j are integers. For a square lattice periodic grating used in this work, the dispersion relation can be transformed to a relation between the resonant wavelengths $\lambda_{i,j}$ and the grating pitch a as:

$$(3) \quad \lambda_{SPP} = \frac{a}{\sqrt{i^2 + j^2}} \sqrt{\frac{\epsilon_m \epsilon_d}{\epsilon_m + \epsilon_d}}.$$

$$(4) \quad \delta_{ij} \approx \left(\frac{\lambda_{ij}}{2\pi}\right) \sqrt{\frac{\text{Re}(-\epsilon_m)}{\epsilon_d}}$$

where $a = a_{x,y}$ and the integers, i and j , correspond to the orders of the 2D grating wave vector in the orthogonal spatial directions. The resonantly generated SPP is a TM mode thus exhibits a dominant electric field component normal to the surface that is the proper polarization for exciting the ISB resonance. At λ_{SPP} the reflectivity of the MHA surface has its lowest value and the intensity of the E_z electric field component at the interface semiconductor metal is enhanced and reaches its maximum.

The study was carried out on a simplified version of a GaN-based QCD that was demonstrated recently. In this alloyed QCD structure the sophisticated multiple QW extractor region is replaced by an AlGaIn thick layer, whose composition is chosen to engineer the internal field and achieve a graded potential. The sample was grown by ammonia molecular beam epitaxy (NH₃-MBE) on an AlN on c-sapphire template. The sample consists of 40 active periods sandwiched between top and bottom Si-doped ($1 \times 10^{19} \text{cm}^{-3}$) Al_{0.6}Ga_{0.4}N contact layers. The active QW consists of 2 nm thick GaN well nominally doped ($2 \times 10^{18} \text{cm}^{-3}$) with Si and left and right AlN barriers with thicknesses of 2 and 1 nm in growth order, respectively followed by extraction region that is formed by a non intentionally-doped 15 nm thick Al_{0.58}Ga_{0.42}N layer. The devices were first processed in the form of $700 \times 700 \mu\text{m}^2$ mesas on a wafer with pre-polished 45° wedge. The mesas have been patterned using standard optical lithography followed by inductively coupled plasma reactive ion etching. Ti/Al/Ti/Au layers were deposited to form the top and bottom contacts layers. The center of the top surface of the mesas was kept unmetallized to allow illumination onto the surface. Schematically cross section of the device is shown in Fig. 1(a). The photocurrent spectra collected with a chopped white near infrared (NIR) light source using a lock-in detection system coupled to the Bruker Equinox 55 Fourier transform IR (FTIR) spectrometer operated in the step-scan mode. The mesa detectors were irradiated onto the surface at 45° angle of incidence and through the 45° polished wedge. The photo-response, measured at room temperature without MHA, was peaked at $1.87 \mu\text{m}$, as

predicted by 8-band k.p calculation using self-consistent Schrödinger-Poisson solver as will be discussed later.

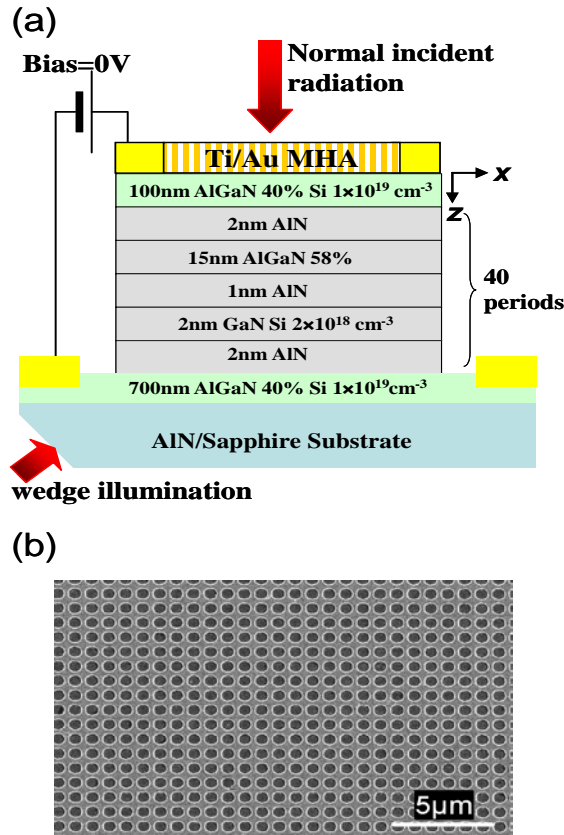


Fig. 1. (Color online) (a) Schematic cross-section structure of the alloyed-QCD with MHA on top of it. (b) Top-down SEM image of the MHA.

Following full characterization (photo response and I-V measurements) of the mesa QCDs, at different light coupling schemes, a second metallization deposition was performed. 5nm Ti and 200nm Au thick layers were deposited on the mesa top surface and patterned with periodic holes using Strata 400 Dual Beam field emission-scanning electron microscope (FE-SEM) and focused ion beam (FIB) system. A zoom-in view SEM image of the MHA is shown in Fig. 1(b). The measured diameter of the hole is $d = 580\text{nm}$ and the period of the array is $a = 835\text{nm}$. For achieving an optimum plasmonic-QCD interaction, the spectral matching of plasmonic resonance to QCD absorption peak and the spatial matching of plasmonic field region to the QCD absorption region must be satisfied. In this work, the diameter and periods of holes array was designed to achieve a plasmon peak resonance at slightly lower energy than the ISB peak resonance. In such a way one can study the effect of the plasmonic resonance on the ISB absorption. The electric field distribution through the active regions of the device was optimized by three dimensional finite difference time domain (FDTD) software (Lumerical). The simulated electric field component intensity distribution of $|E_z|$ at the peak transmission wavelength, $1.82\mu\text{m}$, of the SPP mode (1,0) in the x-y and x-z planes in a unit cell of the MHA is illustrated in Figs. 2(a) 2(b) and 2(c), respectively. The x-y plane in this simulation is at the interface metal/semiconductor 2(b) and at the center of the active region ($z=0.5\mu\text{m}$) 2(a). The hole position in the metallic film is indicated on it by the circle in Figures 2(a) and 2(b). Demonstration the enhancement of $|E_z|$ in the active region due to SPP's generation at the vicinity of the hole is clearly seen in Fig. 2(a) and 2(b). With the increase of the distance from a surface (Fig. 2(b) $z=0$ to Fig. 2(a) $z=0.5\mu\text{m}$) the

localization pattern is smoothed out but the overall symmetry of light above a hole is still determined by the symmetry of scattered SP modes. The depth distribution of $|E_z|$ was simulated and monitored starting from the QCD top contact layer down through the active region on an x-z plane located at $y=0$.

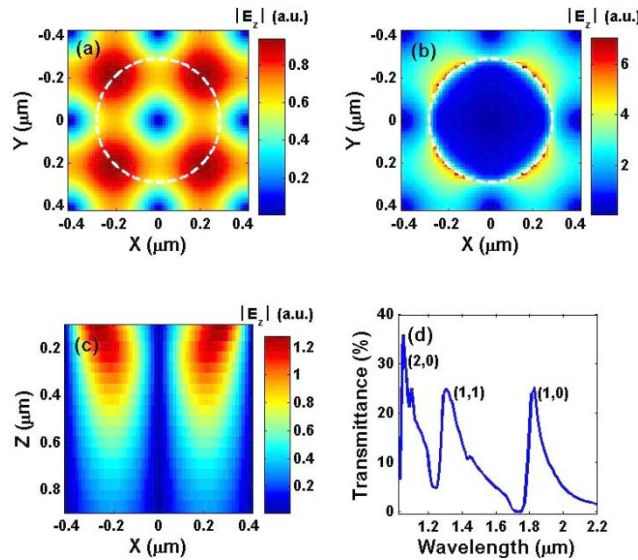


Fig. 2. (Color online) FDTD simulated $|E_z|$ profile for normal incidence from MHA side in (a) the x-y plane at the center of the active region ($z=0.5 \mu\text{m}$) at the peak of transmission wavelength $1.82 \mu\text{m}$ and at $z=15 \text{ nm}$ (b). $z=0$ denotes the interface of the metallic film and the sample. (c) $|E_z|$ in the x-z plane at $y=0$ at peak transmission wavelength. The hole position is indicated with a dashed circle in (a) and (b).

As illustrated in Fig. 2(c), this component of the electric field spreads over to more than $1 \mu\text{m}$ below the metallic film, covering completely the active region. These results predict that the active region of the QCD efficiently receives a substantial p (TM polarized) component of the incident electric field. Figure 2(d) shows simulated near field (at the interface GaN/MHA) transmission of 200 nm Ti/Au MHA on $1 \mu\text{m}$ GaN sample. (I,J) are plasmon mode numbers.

3. Experimental Results

Fig. 3 shows the far field FTIR transmission spectrum of a reference sample consists of $300 \mu\text{m}$ sapphire/ $2 \mu\text{m}$ AlN with Ti(5 nm)/Au(200 nm) MHA as described above. The experimentally measured resonances demonstrate good agreement with the theoretically simulated transmission spectra as shown in Fig. 2(d) where one can see that the SPP mode (1,0) peak resonance, λ_{SPP} , is at $1.82 \mu\text{m}$. The dips and asymmetric shape of the transmission spectrum of the reference MHA sample have been reported and is attributed to the Fano-type interference between discrete plasmonic resonance and the radiative damping of plasmons due to surface plasmon scattering on the hole arrays. We attribute the background transmission in the far field measurement at Fig. 3 to non-resonant and scattering of the field through the subwavelength holes according to Bethe's solution to the problem of direct transmission of the electromagnetic field through an infinitely thin ideal metal with sub wavelength holes.

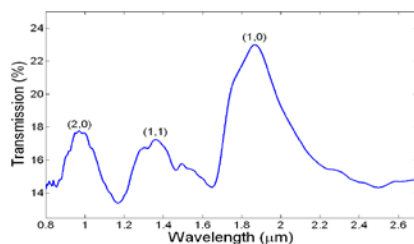


Fig. 3 The measured (far field) relative transmission spectrum of a 200 nm Ti/Au MHA on AlN($1 \mu\text{m}$)/sapphire ($300 \mu\text{m}$) reference sample. (I, J) are plasmon mode numbers.

The spectral response of the device was

carried out at room temperature and zero bias using (FTIR) spectrometer with CaF_2 beam splitter and Tungsten NIR source. In order to quantify the performance improvement of the integrated device, preliminary photoresponse measurements of the device *without* MHA were taken in standard configurations, i.e. illumination through the top facet at normal incidence, at 45° angle of incidence and onto a 45° polished wedge.

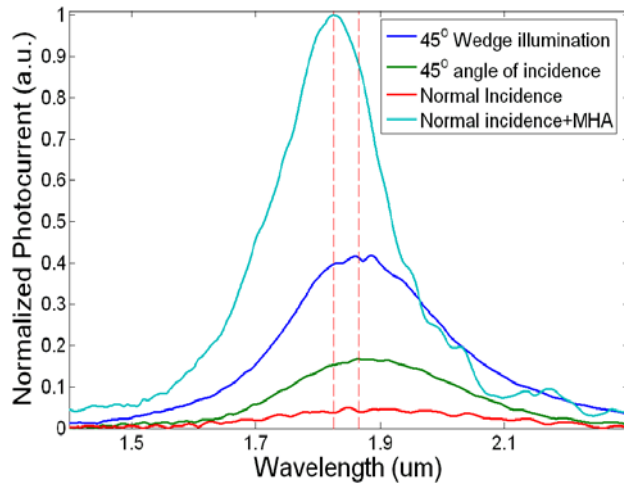


Fig. 4. Normalized photocurrent spectral intensities of the alloyed-QCD device with and without MHA at different illumination schemes. The vertical dashed lines indicate the shift in peak position of the device; before fabrication of MHA on top of the QCD (left line) and after (right line). The spectra are normalized with the illumination area. All measurements were done at zero bias and at room temperature.

Figure 4 shows the normalized (to optical area of the different light illumination schemes) photoresponse spectra of QCD without MHA measured in standard 45° polished wedge configuration (continuous blue line) and 45° angle illumination on the top surface (continuous green line). The two spectrums peaked at $1.87 \mu\text{m}$ with full width at half maximum (FWHM) of $0.3 \mu\text{m}$. The photoresponse spectrum of the same QCD with the MHA under normal incidence illumination (red line) is peaked at $1.82 \mu\text{m}$, which corresponds to the designed plasmon peak resonance wavelength ((1,0) peak resonance shown in Fig. 3) and the FWHM is smaller ($0.19 \mu\text{m}$) compared to the QCD photoresponse spectrum without MHA. As expected the photoresponse of the 45° wedge illumination is 2-3 time larger than 45° top surface illumination due to different coupling factor $\sin^2(34.5)/\cos(34.5)$ or $\sin^2(18)/\cos(18)$ respectively. The normal incidence responsivity of the QCD-MHA device shows strong enhancement (2-3 times) compares to reference QCD, with out MHA, at 45° light coupling schemes. The normal incidence photoresponse spectrum of the QCD, before MHA deposition, is shown by red line in Fig. 4. We attribute the small signal at normal incidence (theoretically not allows) in the reference QCD to stray light scattering from the mesa surfaces. The large difference (factor 10) between the two signals at normal incident reflects the rotation of polarization and absorption enhancement by the MHA induced SPP.

The photo response spectra and DC dark current-voltage characteristics were measured in a wide range of temperatures using a closed cycle He cryostat and HP semiconductor analyzer.

For the accuracy of characterization, the responsivity of the device was estimated using two different techniques: calibrated black body at 1000 K and super continuum tunable laser source that was focused at normal incidence, at the peak wavelength ($\lambda=1.82\mu\text{m}$) on the device top surface. It was found that the absolute responsivity of the QCD with MHA at its peak wavelength of $1.82 \mu\text{m}$ is $\sim 2 \text{ mA/W}$ at normal

incident illumination and at room temperature. The measured values for absolute responsivity of the QCD without MHA at its peak wavelength of 1.87 μm are 0.7 mA/W and 0.22 mA/W for 45° for polished wedge illumination and 45 angle front illumination on the top surface, respectively. The performance of photodetectors is usually expressed by the specific detectivity D^* . We assumed that Johnson detectivity is the dominant component for the total detectivity at room temperature and at zero bias. The Johnson noise limited detectivity, D_J^* , was calculated by

$$D_J^* = R_p \sqrt{\frac{R_0 A}{4k_B T}} \quad (5)$$

where R_p is the peak responsivity deduced from measured photocurrent response. $R_0 A$ is the resistance area product at zero bias extracted from the I-V-curves, k_B is the Boltzmann constant and T is the temperature. Using this equation we found that the detectivities of QCD with MHA is about 5×10^8 Jones at 300 K and 2×10^{10} Jones at 90 K (assuming 300 K background and hemispheric field of view).

Discussion and analysis

The photoresponse, R_i , of a QCD can be expressed as :

$$R_i = \frac{I_{photo}}{h\nu\Phi} = a \times \eta \times \frac{1}{h\nu} \quad (6)$$

where $h\nu$ is the intersubband energy expressed in eV, Φ is the amount of incident photon number per unit time, a the absorption per one QW, η is the electron extraction efficiency, i.e., the probability of photo excited electrons to transit into the extractor towards the next active QW. The absorption per one QW is related to the carrier concentration in the ground state and to the light coupling scheme by the following:

$$a = \sigma_{TM} \frac{\sin^2(r)}{\cos(r)} n_{2d} \quad (7)$$

and

$$\sigma_{TM} = \frac{I_{photo}}{\Phi n_{2D} \eta \left(\frac{\sin^2(r)}{\cos(r)} \right)} \quad (8)$$

where σ_{TM} is the absorption cross section for TM-polarized light and r is the refraction angle inside the active region (34.5° in the sapphire/AlN multipass geometry), n_{2D} is the electron surface concentration in the ground state in the active QW. We assume that the extraction efficiency η and the incident radiation intensity Φ are the same for 45° edge QCD, reference device, and for the QCD-MHA at normal incidence illumination. Nevertheless, with respect to amount of photons entering into the device due to different transmittances, light coupling efficiency and the light pass length in the active part the two QCD configurations are different. To quantify the performance enhancement by the QCD-MHA design we normalized the absorption cross section ratio of the QCD-MHA to the 45° edge reference QCD at peak wave length by:

$$\frac{\sigma_{TM}(MHA)}{\sigma_{TM}(45^\circ)} = \frac{I_{photo}(MHA)T(45^\circ)\sin^2(34.5^\circ)/\cos(34.5^\circ) \times 2}{I_{photo}(45^\circ)T(MHA)} \quad (9)$$

where $I_{photo}(MHA)$ and $I_{photo}(45^\circ)$ are the normalized photoresponse signal respectively, $T(45^\circ)$ is the transmittance through the interface air/sapphire in 45° edge device $\approx 70\%$, gained from Fresnel formula), $\sin^2(34.5^\circ)/\cos(34.5^\circ)$ is the light coupling to ISB efficiency at the sapphire/AlN interface. For the QCD-MHA device with normal incidence illumination we assume at Eq. 9 maximum 100% coupling efficiency (complete polarization conversion). The transmittance through the MHA, $T(MHA)$, was estimated from the simulated calculations or from the experimental far field transmission measurements to be in the range of 8% to 25% (Fig.3). The factor 2 at the nominator compensates the double pass of incident light in the 45° edge configuration compare to single pass in the QCD-MHA normal incident configuration. Taking all these factors into account we will find that the plasmonic enhanced absorption cross section for TM light-polarization (which is proportional to QW absorption quantum efficiency) enhanced by a factor 6 to 17 (depends on the estimated transmittance value of the MHA mask shown in Fig. 3) in comparison to "standard" absorption cross section.

Additional demonstration to the effect of MHA on absorption cross section is the comparison of normalized absorption in wedge configuration and in normal incident illumination through metal hole array. We first measured the transmission of a second sample with 40 periods alloy QCD structure using FTIR spectrometer in multipass geometry. The number of passes within the active region is 18. Fig. 7 shows (black line) the normalized absorption ($\log(S \text{ polarization}/P \text{ polarization})$) spectrum, which reveals absorption peaked at $1.76 \mu\text{m}$ (0.7 eV) with a full width at half maximum of 140 meV. Following the wedge transmission measurement, metal hole array Ti/Au (diameter 560 nm and period 800 nm) was deposited on top surface of the QCD sample using E-Beam lithography and lift of process. The transmission of the sample with MHA was measured in vertical incident illumination and normalized by the transmission of same sample with out MHA. Clear absorption peak (blue line) at $1.8 \mu\text{m}$ (0.69 eV) with (60 meV FWHM) is shown in Fig.7. This measurement demonstrates nicely the TM-polarized characteristics of the coupled surface plasmon polariton –intersubband resonance absorption. Taking into account that the sample structure in the measurements is the same we can write simple equation for the cross section ratio:

$$\frac{Absorbance(MHA)}{Absorbance(45^\circ)} = \frac{\sigma(MHA)T(MHA)}{\sigma(45^\circ)\sin^2(34.5^\circ)/\cos(34.5^\circ)N \cdot T(45^\circ)} \quad (10)$$

where $Absorbance(MHA)$ and $Absorbance(45^\circ)$ are the area under the lines in Fig. 7. $N=18$ is the number of passes in wedge configuration, $\sin^2(34.5^\circ)/\cos(34.5^\circ)$ is the electric field coupling factor in wedge configuration and $T(MHA)$, $T(45^\circ)$ are the transmittance of normal incident light on sapphire and on MHA/GaN respectively. If we will take $T(45^\circ) = 70\%$ (from literature) and $T(MHA)=20\%$ (from Fig. 2.d) we will find enhancement of factor 7 in the TM cross section for absorption when using normal incident MHA configuration. These results are about the same to those extracted from the photoresponse measurements.

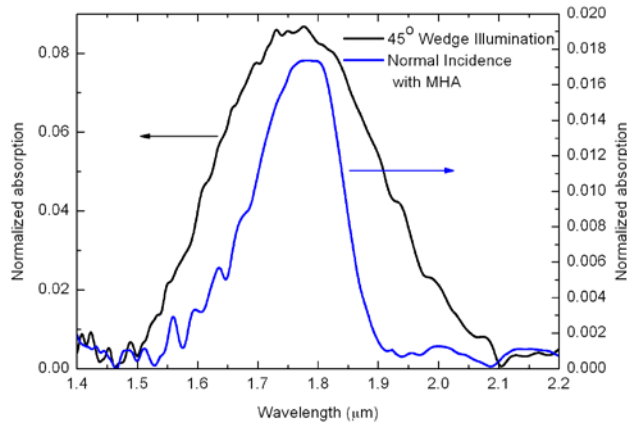


Fig. 7 Measured absorbance spectra of 40 periods QCD sample at room temperature in 45° wedge waveguide configuration (black line) and in normal incident illumination on metal hole array (blue line).

The interaction of light with nanostructured metals has been studied extensively in recent years. The resulting near-field optical intensity can be two to three orders of magnitude higher than the incident intensity. The near-field distribution of light over a surface under the enhanced transmission conditions reveals the strongly localized spots of high intensity. In the localization spots the intensity enhancement of up to 500-3000 times is observed theoretically and experimentally. However, very little research has been carried out into the interaction of these strong near fields with semiconductors and the further transformation of the optical energy into electricity.

Optical antenna as a nanophotonic structure can convert light into near field optical mode by means of surface plasmon polariton. Using optical antenna terminology we can formally relate the antenna aperture to absorption cross-section. Let us consider the intersubband absorption as a dipole-like receiver with cross-section σ_0 when it is not coupled to an antenna. Once we couple the receiver to an optical antenna (the MHA), the field at the receiver increases to \mathbf{E} and the cross-section or antenna

aperture becomes $\sigma = \sigma_0 \left| \frac{\mathbf{d} \cdot \mathbf{E}}{\mathbf{d} \cdot \mathbf{E}_0} \right|$ where \mathbf{d} is the electronic dipole moment, \mathbf{E}_0 is the

incident electromagnetic field at the receiver location. Thus, the aperture of an optical antenna (absorption-cross section) scales with the local intensity enhancement factor. We attribute the large absolute resonant absorption enhancement to the confinement of electromagnetic field at the sub-wavelength volume.

In conclusion, we demonstrated a normal-incident quantum cascade detector excited by surface plasmons resonance using Ti/Au MHA integrated on top surface of the detector active region. We report on a resonant enhancement of responsivity in comparison to 45° edge illumination due to combined effect of polarization conversion and strong increase in the absorption quantum efficiency due to enhance density of photon states induced by localized plasmons electric field. Future research on this topic will include optimization of doping in the active QW that could enhance the absorption by one order of magnitude. In addition, more efficient light coupling scheme like backside-illumination and cavity resonant structure will pave the way for practical applications in the near future.

5. Summary and Outlook

The project resulted in deep and through understanding of the spectral and enhancement features of metamaterials based on arrays of antennas made of nanoplasmonic structures. As a result of this research – accurate designs of such antennas across the red visible to SWIR regimes is affordable using geometry and coupling mechanisms – including broadband antennas based on breaking the rules of regular coupling mechanisms.

The second facet of this research examined the basic concepts of embedding of such antenna arrays with semiconductor devices – for enhanced performance. We showed successful engagement of antenna arrays with photovoltaic solar cells, light emitters and detectors – and in all we achieved the desired enhancement (in energy collection, in emission speed and in detector detectivity respectively). We are still looking at the fundamental issues related to the very close proximity of the semiconductor active layer or structure to the metallic nanoantenna – as a major issue to understand and mitigate for efficient plasmonic-enhanced real-world devices.

Based on our study – we strongly believe that the incorporation of antenna based metamaterial in detecting and emitting devices will be one of the few applicative fields emerging from the metamaterial studies – when very small and power efficient devices are essential. However – still we are facing basic issues in this combination that must be resolved. We are looking now intensively into understanding and solving these issues.

6. Publications resulting from the project

Peer reviewed journal and conferences proceedings

1. N. Berkovitch, P. Ginzburg, and M. Orenstein, "Concave Plasmonic Particles for Extreme Tunability in the Near Infra-Red", *Nanoletters* 10 pp. 1405–1408 (2010).
2. A. Normatov, P. Ginzburg, N. Berkovitch, G. M. Lerman, A. Yanai, U. Levy and Meir Orenstein "Efficient Coupling and Field Enhancement for Nano-Scale: Plasmonic Needle", *Optics Express* 18, pp. 14079-14086 (2010).
3. A. Normatov, N. Berkovitch, P. Ginzburg, G. M. Lerman, A. Yanai, U. Levy and M. Orenstein, "Nano-Coupling and Enhancement in Plasmonic Conical Needle", CLEO, San Jose, Ca USA (2010)
4. P. Ginzburg, N. Berkovitch, A. Normatov, G. M. Lerman, A. Yanai, U. Levy M. Orenstein "Field Enhancement By Efficient Nano-coupling To Plasmonic Conical Needle", Fronteer in Optics, paper FWN6, Rochester NY USA (2010)
5. P. Ginzburg, A. Nevet, N. Berkovitch, A. Normatov, G. M. Lerman, A. Yanai, U. Levy, and Meir Orenstein, "Plasmonic resonance effects for tandem receiving-transmitting nano-antennas", *NanoLetters* 11, pp. 220-224 (2011)
6. I. Diukman, L. Levi, N. Berkovitch, N. Tessler and M. Orenstein "Enhanced absorption in organic photovoltaic cells by patterned Au nano disks embedded in the active layer", *Optics Express* 19, pp. A64-A71 (2011)
7. P. Ginzburg, N. Berkovitch, A. Nevet, I. Shor, and M. Orenstein "Resonances On-Demand for Plasmonic Nano-Particle", *NanoLetters* 11 pp. 1329-1333 (2011).
8. N. Berkovitch, and M. Orenstein "Thin wire shortening of plasmonic nanoparticle dimers: the reason for red shifts", *NanoLetters* 11, pp. 2079-2082 (2011).
9. D. Arbel, N. Berkovitch, A. Nevet, A. Peer, D. Ritter and M. Orenstein, "Light emission rate enhancement from InP MQW by plasmon nano-antenna arrays", *Opt. Ex.* 19, pp. 9807-9813 (2011)
10. I. Diuckman and M. Orenstein, "Absorption enhancement mechanisms in Silicon solar cells – by Plasmonic nanostructures", *Solar Energy Materials & Solar Cells* 95, pp. 2628-2631 (2011)
11. N. Berkovitch, P. Ginzburg, M. Orenstein, "Nano plasmonic antennas in the NIR regime", *J. Phys.: Condes. Matter* 24, 073202 (2012) **Invited Review Paper.**
12. M. Orenstein, "The role of slow light on hyperbolic metamaterials and plasmonic nano antennas", Photonics West, San Francisco, Ca, USA (2011) **Invited talk**
13. M. Orenstein, "Optical - Nanoantennas -The new Addition to the Photonics Arsenal" Nano-S&T, Dalian, China (2011) **Invited talk**
14. M. Orenstein, "Metamaterials based on nanoantennas", Villa Conference on Metamaterials (VCM 2011) Las Vegas, Nevada, USA (2011) **Invited talk**
15. P. Ginzburg, I. Shor, N. Berkovitch, A. Nevet, M. Orenstein, "On-demand Engineering of Multiple Resonances of Plasmonic Particles", paper THU2s.4, International Topical meeting on Nanophotonics and Metamaterials, Seefeld, Austria (2011)
16. P. Ginzburg, A. Nevet, N. Berkovitch, A. Normatov, G. M. Lerman, A. Yanai, U. Levy, M. Orenstein, "Tandem of Plasmonic Nano-antennas for Resonant Scattering Enhancement", paper WED5s.4, International Topical meeting on Nanophotonics and Metamaterials, Seefeld, Austria (2011)
17. I. Dukman, L. Tzabari, M. Orensteain, N. Tessler, "Organic photovoltaic cells - enhanced absorption by patterned Au nano disks in the active layer", paper WED4f.22,

International Topical meeting on Nanophotonics and Metamaterials, Seefeld, Austria (2011)

18. N. Berkovitch, M. Orenstein, "Wire connected plasmonic nanoparticles", paper Tue4f.65, International Topical meeting on Nanophotonics and Metamaterials, Seefeld, Austria (2011)

19. N. Berkovitch, P. Ginzburg, M. Orenstein, "Plasmonic metamaterials in the near infrared: large tunability by concave unit cells", paper Tue4f.20, International Topical meeting on Nanophotonics and Metamaterials, Seefeld, Austria (2011)

20. P. Ginzburg, I. Shor, A. Nevet, N. Berkovitch and M. Orenstein, "Plasmonic Particles with Engineered Resonances – Superfilters and Superabsorbers", CLEO QELS, paper QTuG6, Baltimore Md, USA (2011).

21. D. Arbel, N. Berkovitch, A. Nevet, and M. Orenstein, "Plasmon Nano-Antenna Enhanced Light Emission from InP MQW- Towards faster LEDs", CLEO QELS, paper JMF5, Baltimore Md, USA (2011).

22. I. Diukman, L. Tzabari, N. Berkovitch, N. Tesler and M. Orenstein, "Patterned Plasmonic Nano-Antennas Embedded in the Active Layer of Organic Photovoltaic Cells – Enhanced Absorption", CLEO QELS, paper CMCC2, Baltimore Md, USA (2011).

23. D. Arbel, N. Berkovitch, A. Nevet, and M. Orenstein, "Towards faster LEDs: Plasmon Nano-Antenna Enhanced Emission Rate from InP MQW at Telecommunications Wavelength", SPP5, Busan, Korea (2011).

24. N. Berkovitch, and M. Orenstein, "Plasmonic nanoparticles connected by conductive bridge", SPP5, Busan, Korea (2011).

25. N. Berkovitch, P. Ginzburg and M. Orenstein, "Large tunability by concave plasmonic particles in the Near Infrared", SPP5, Busan, Korea (2011).

26. P. Ginzburg, A. Nevet, N. Berkovitch, A. Normatov, G. M. Lerman, A. Yanai, U. Levy, M. Orenstein, "Scattering enhancement by coupled plasmonic nano-antennas", SPP5, Busan, Korea (2011).

27. P. Ginzburg, I. Shor, A. Nevet, N. Berkovitch and M. Orenstein, "Design of plasmonic particles with pre-determined resonance spectrum", SPP5, Busan, Korea (2011).

28. M. Orenstein, "Metamaterials based on nanoantennas", Photonics West, San Francisco, Ca, USA (2012) **Invited talk**

29. M. Orenstein, "Metamaterials based on nanoantennas", Villa Conference on Metamaterials (VCM 2011) Orlando, Fl, USA (2012). **Invited talk**

30. M. Orenstein, "Particle based nanoantennas", Gordon Conference on Plasmonics, Colby College, Me, USA(2012). **Invited talk**

31. M. Orenstein "Light emission from nanometals", Photonic Devices and Applications: Metallic Nanoplasmonics, San Diego, Ca, USA (2012) **Invited talk**

32. L. Gal, N. Berkovitch, M. Orenstein, "Elliptic-Hyperbolic plasmonic antennas and their radiation patterns", paper QM4hH, CLEO, San Jose, Ca (2012).

33. A. Yanai, M. Orenstein and U. Levy, "Giant resonance and absorption in ultrathin metamaterial", paper QTh1A, CLEO, San Jose, Ca (2012)

34. N. Berkovitch, M. Orenstein, "Broad-band plasmonic nanoantennas", paper JTh2A.85, CLEO, San Jose, Ca (2012).

35. M. Orenstein, "Metamaterials based slow light", Photonics West, San Francisco, Ca (2013) **Invited talk**

36. M. Orenstein, "Plasmonic Sources and detectors for interconnect", Photonics Devices and Applications: Metallic Nanoplasmonics, San Diego, Ca (2013) **Invited talk**

37. A. Pesach, S. Sakr, E Giraud, M. Tchernycheva, M Orenstein, N. Grandjean, F. Julien, G Bahir, " Plasmonic-Polarization Enhancement of Novel GaN/AlN Quantum Cascade Detector", paper CM3F.4, CLEO, San Jose, Ca (2013).
38. A. Pesach, S. Sakr, E Giraud, M. Tchernycheva, M Orenstein, N. Grandjean, F. Julien, G Bahir, "Normal-incident plasmonic enhanced GaN/AlN quantum cascade detector" 2th International Conference on intersubband transitions in quantum wells, NY (2013)